ORIGINAL ARTICLE

SIRT1 maintains bone homeostasis by regulating osteoblast glycolysis through GOT1

Xinxin Jin[1] · Xulei Sun[2] · Xiao Ma[2] · Zixuan Qin[1] · Xin Gao[1] · Xiaomin Kang[2] · Huixia Li[1] · Hongzhi Sun[1]

Abstract

The silent information regulator T1 (SIRT1) is linked to longevity and is a crucial mediator of osteoblast function. We investigated the direct role of *Sirt1* during bone modeling and remodeling stages in vivo using Tamoxifen-inducible osteoblast-specific *Sirt1* conditional knockout (cKO) mice. cKO mice exhibited lower trabecular and cortical bone mass in the distal femur. These phenotypes were coupled with lower bone formation and bone resorption. Metabolomics analysis revealed that the metabolites involved in glycolysis were significantly decreased in cKO mice. Further analysis of the quantitative acetylome revealed 11 proteins with upregulated acetylation levels in both the femur and calvaria of cKO mice. Cross-analysis identified four proteins with the same upregulated lysine acetylation site in both the femur and calvaria of cKO mice. A combined analysis of the metabolome and acetylome, as well as immunoprecipitation, gene knockout, and site-mutation experiments, revealed that *Sirt1* deletion inhibited glycolysis by directly binding to and increasing the acetylation level of Glutamine oxaloacetic transaminase 1 (GOT1). In conclusion, our study suggested that *Sirt1* played a crucial role in regulating osteoblast metabolism to maintain bone homeostasis through its deacetylase activity on GOT1. These findings provided a novel insight into the potential targeting of osteoblast metabolism for the treatment of bone-related diseases.

Keywords Conditional knockout · Deacetylation · Bone mass · Bone formation

Abbreviations

SIRT1	Silent information regulator T1
TM	Tamoxifen
cKO	Conditional knockout
GOT1	Glutamine oxaloacetic transaminase 1
BV/TV	Bone volume per tissue volume
Tb.N	Trabecular number
Tb.Th	Trabecular thickness
Tb.Sp	Trabecular separation
Ct.Th	Cortical thickness
Tt.Ar	Total cortical area
H&E	Hematoxylin–eosin
TRAP	Tartrate-resistant acid phosphatase
ELISA	Enzyme-linked immunosorbent assay
RT-qPCR	Real-time quantitative PCR
ALP	Alkaline phosphatase
IP	Immunoprecipitation
AOA	Aminooxyacetic acid
PBM	Peak bone mass
Tb.Ar	Trabecular bone area
Tb.Ad	Average distribution of trabecular bone
Tb.N	Trabecular osteoblast number
MAR	Mineral apposition rate
BFR/BS	Bone formation rate per bone surface
PINP	Procollagen I N-terminal propeptide
Col1a1	Collagen1 α1
Alpl	Alkaline phosphatase
Bglap	Bone gamma carboxyglutamate protein
Nfatc1	Nuclear factor of activated T cells, cytoplasmic, calcineurin-dependent 1
Itgb3	Integrin beta 3
Ctsk	Cathepsin K
Dcst	DC-STAMP domain-containing 1

Correspondence to Hongzhi Sun sunhongzhi@mail.xjtu.edu.cn;
Xinxin Jin jxx20200311@xjtu.edu.cn".

✉ Xinxin Jin
  jxx20200311@xjtu.edu.cn

✉ Hongzhi Sun
  sunhongzhi@mail.xjtu.edu.cn

1 Department of Physiology and Pathophysiology, School of Basic Medical Sciences, Xi'an Jiaotong University Health Science Center, Xi'an 710061, Shaanxi, China

2 Center for Translational Medicine, The First Affiliated Hospital of Xi'an Jiaotong University, Xi'an 710061, Shaanxi, China

ACP5	Acid phosphatase 5, tartrate resistant
CTX-1	C-terminal telopeptide of type-1 collagen
TCA	Tricarboxylic acid
G6P	Glucose-6-phosphate
F6P	Fructose-6-biphosphate
F-1,6-P	Fructose-1,6-biphosphate
2-PGA	2-Phosphoglycerate
PEP	Phosphoenolpyruvate
ATP	Adenosine triphosphate
G1P	Glucose-1-phosphate
DHAP	Dihydroxyacetone phosphate
R-1,5-P	Ribose 5-phosphate
6PG	6-Phosphogluconate
TPP	Thiamine pyrophosphate
AMP	Adenosine monophosphate
ADP	Adenosine diphosphate
GDP	Guanosine diphosphate
GTP	Guanosine triphosphate
PPP	Pentose phosphate pathway
Kac	Lysine acetylation
KSCP	Kac site-changed proteins

Introduction

Bone integrity and homeostasis are orchestrated by the dynamic process of bone remodeling, in which a continuous cycle of old bone is replaced by newly formed bone throughout life [1, 2]. This process is regulated by two principal bone cells: osteoblasts and osteoclasts. Osteoblasts, which originate from the mesenchymal lineage, produce bone collagen matrix and regulate its mineralization, are responsible for bone formation [3]. Osteoclasts, which arise from the hematopoietic lineage, are responsible for bone resorption [3]. Osteoblasts synthesize and mineralize new bone matrix to fill the osteoclast excavated prior to resorption pits, which makes the bone formation and the bone resorption coupled at the temporal, spatial, and quantitative levels to maintain a delicate balance of bone remodeling [3]. Dysfunction in those two main cell types leads to bone remodeling disruption, thus changing the bone microarchitecture, which is the pathological basis of bone-related disorders, such as osteoporosis, Paget's disease, and osteolysis [4].

Sirtuin-1 (SIRT1), a unique nicotinamide adenine dinucleotide NAD$^+$-dependent deacetylate, is one of the most conserved members of the seven mammalian sirtuin family members [5, 6]. SIRT1 regulates various physiological and pathological cellular processes, such as the DNA damage response, autophagy, metabolism, and aging [5, 6]. Based on these functions, SIRT1 has been implicated in activating survival pathways and extending lifespan, thus preventing and treating senescence and aging-related diseases, such as cancer, neurodegeneration, and cardiovascular diseases [7, 8].

Indeed, SIRT1 and its targeted drugs have emerged as therapeutics against bone-related diseases, especially osteoporosis [9, 10]. Using Prx1-Cre, Osx-Cre, or Col1a1-Cre mice, targeted deletion of *Sirt1* in the osteoblastic lineage and their descendants, beginning at the embryonic period, revealed that *Sirt1* played essential roles in regulating bone homeostasis [11–14]. Increasing evidence has suggested that SIRT1 regulates transcription, translation, post-translation modification, and protein stability by protein–protein interactions in the osteoblastic lineage [15–17]. However, the underlying mechanisms of how *Sirt1* modulates the functions of osteoblasts to impact bone homeostasis remain unclear.

During bone remodeling, osteoblasts require sufficient energy to produce and secrete large amounts of extracellular matrix to regulate bone formation [18–20]. Glycolysis is one main energy source for osteoblast differentiation and function regardless of oxygen conditions [18–22]. Although a few studies have reported the relationship between *Sirt1* and glycolysis [23–26], how *Sirt1* controls glycolysis in osteoblasts is poorly studied. Glutamine oxaloacetic transaminase 1 (GOT1), a pyridoxal phosphate-dependent enzyme, is mainly localized in the cytoplasm [27]. It is multifunctional, reversely governs the Asp-malate shuttle and catalyzes the glutamate and α-ketoglutarate (α-KG) conversion, thereby playing vital roles in cell metabolic reprogramming in cancers [27]. Emerging evidence has reported that GOT1 is also an important glycolytic enzyme that regulate the glycolysis pathway [28–30]. However, in osteoblasts, whether GOT1 drives glycolysis metabolic pathways and whether GOT1 is the substrate target of SIRT1 in regulating glycolysis needs to be further studied.

In this study, postnatally targeted deletion of *Sirt1* by utilizing Col1a-cre/ERT2 mice, we found that *Sirt1* regulated glycolysis through deacetylation of GOT1 in osteoblasts to maintain bone homeostasis.

Materials and methods

Animal studies

Sirt1$^{flox/flox}$ mice were gifted by Prof. Gao Xiang of Nanjing University (Nanjing, China) [31]. B6.Cg-Tg (Col1a-Cre/ERT2)1Crm/J mice (Stock No. 016241) were obtained from Jackson Laboratory (Bar Harbour, ME, USA) [32]. Rosa26-LSL-Tdtomato (Stock No. C001181) and Rosa26-mTmG (Stock No. C001192) mice were purchased from Cyagen Biosciences Inc. (Guangzhou, China). All the mice used in our study were from a pure C57BL/6 background. Mice were maintained in the SPF animal laboratory at Xi'an Jiaotong University. All mice had free access to food and water, and the cages and bedding were changed once a week.

Mouse breeding and tamoxifen (TM) administration

For mouse breeding, the *Sirt1*$^{flox/flox}$ mice (F0 generation) and Col1a-Cre/ERT2 (F0 generation) mice were crossed to obtain the *Col1a-Cre/ERT2; Sirt1*$^{flox/−}$ mice (F1 generation), and then the *Col1a-Cre/ERT2; Sirt1*$^{flox/−}$ mice (F1 generation) were intercrossed with *Sirt1*$^{flox/flox}$ mice (F0 generation) to finally generate TM-inducible *Col1a-Cre/ERT2; Sirt1*$^{flox/flox}$ mice (F2 generation). The *Col1a-Cre/ERT2; Sirt1*$^{flox/flox}$ mice were viable and fertile without TM induction. TM (Sigma, T5648) was used to induce *Sirt1* knockout. Briefly, TM (0.2 mg/mouse) was intraperitoneally injected into mice at postnatal days 5, 7, 9, and 11 until dissection at 8 weeks. For adult mice, TM (75 mg/kg) was intraperitoneally injected daily for 5 consecutive days at 8 weeks mice until dissection at 16 weeks. For consistency, the *Col1a-Cre/ERT2; Sirt1*$^{flox/flox}$ mice and littermate *Sirt1*$^{flox/flox}$ mice received identical amounts of TM. In our following study, the *Col1a-Cre/ERT2; Sirt1*$^{−/−}$ mice were designated cKO mice, and the *Sirt1*$^{flox/flox}$ mice were designated control mice.

Similarly, TM-inducible *Col1a-Cre/ERT2; Sirt1*$^{flox/flox}$; Rosa26-LSL-Tdtomato mice and TM-inducible *Col1a-Cre/ERT2; Sirt1*$^{flox/flox}$; Rosa26-mTmG mice were generated by breeding *Col1a-Cre/ERT2; Sirt1*$^{flox/flox}$ mice with Rosa26-LSL-Tdtomato mice or Rosa26-mTmG mice, respectively.

Mice genotyping

Genomic DNA from mouse tail snips was extracted using the Mouse Direct PCR Kit (Bimake, B40015 and B45012). Genomic DNA of other tissues (heart, liver, spleen, lung, kidney, skull, and femur) was extracted using a DNeasy blood and tissue kit (Qiagen, 9504). Genotyping was performed by PCR using the primers shown in Supplementary Table 1. For the *Sirt1* gene, 550 bp was detected in the WT mice, 750 bp was detected in the mutant mice, and both 550 bp and 750 bp were detected in the heterozygous mice. For the Col1a1 gene, 500-bp was detected in the mutant mice, and 460 bp was detected in the WT mice. For the tomato gene, 196 bp was detected in the mutant mice, and 297 bp was detected in the WT mice. For the mTmG gene, 300 bp was detected in the mutant mice, and 428 bp was detected in the WT mice.

Micro-CT

The collected femur samples were scanned under micro-CT (Aoying Testing Technology, AX2000) at 80 kV voltage, 60 μA current, 5.9 μm resolution, and 500 ms exposure time. For the femurs, the edge of the region of interest (ROI) was chosen to be approximately 1–1.5 mm thick underneath the growth plate. The scanned images were analyzed by VG Studio MAX 3.4 software. Quantification of trabecular and cortical bone was performed, including bone volume fraction (BV/TV), trabecular thickness (Tb.Th), trabecular number (Tb.N), trabecular separation (Tb.Sp), cortical thickness (Ct.Th), and total cortical area (Tt.Ar).

Calcein green staining

The control and cKO mice were intraperitoneally injected with 20 mg/kg calcein green (Sigma, C0875) 10 days and 7 days before euthanization. The femurs were isolated from mice after euthanasia, fixed in 4% paraformaldehyde for 48 h, and then decalcified according to the rapid decalcifier operational manual (Shanghai Lushen Co., Ltd., Vcare DC-6505) for 1 week. Afterwards, the decalcified femurs were embedded in paraffin and cut into 4 μm sections. The sections were then photographed by an inverted fluorescence microscope (Nikon Ti-S, Tokyo, Japan). The bone formation rate (BFR/BS) and mineral apposition rate (MAR) of the trabecular and cortical bone in the pictured images were analyzed by ImageJ software (1.52a, Inc., MD, USA).

Histochemistry staining

The collected femurs were fixed in 4% paraformaldehyde for 48 h, decalcified in EDTA for 14 days, embedded in paraffin and cut into 4 μm thick sections for hematoxylin–eosin (H&E) (Beyotime, C01055) and tartrate-resistant acid phosphatase (TRAP) (Solarbio, G1492) staining. The images were captured by the BA210 digital camera, and three images in each section were analyzed by Motic Images Advanced 3.2 software.

Immunofluorescence staining

Paraffin sections were dewaxed to water, and then antigen retrieval was performed using citric acid buffer (pH 6.0). After being blocked with goat serum, the tissues were incubated with appropriate primary and secondary antibodies, and stained with DAPI. Finally, the sections were sealed with an anti-fluorescence quencher. The primary antibodies were SIRT1 (Abcam, ab110304) (1:100), BGLAP (Santa Cruz, sc-376726) (1:100), and ACP5 (Abcam, ab191406) (1:100). The secondary antibodies were CY3 (Servicebio, GB21301) (1:100) and FITC (Servicebio, GB22303) (1:100). The images were captured at 600x, and three fields of view of each section were acquired. Images were captured using CaseViewer 2.4 software (3DHISTECH, Hungarg) and OlyVIA software (OLYMPUS, Japan). The positively stained areas were analyzed using a Halo 101-WL-HALO-1 system (Indica labs, U.S.A) and ImageJ software (1.52a, Inc., MD, USA).

Enzyme-linked immunosorbent assay (ELISA)

ELISA was performed in accordance with the instructions of several mouse ELISA kits: PINP (MEIMIAN, MM-43891M2), CTX-1 (MEIMIAN, MM-43891M2), G6P (Shanghai Yuanxin Biotech, *Co., Ltd.*, YX-W-6PG), F6P (Shanghai Yuanxin Biotech, *Co., Ltd.*, YX-060616M), F-1,6-P (Shanghai Yuanxin Biotech, *Co., Ltd.*, YX-C-B207), 2-PGA (COIBO BIO, *Co., Ltd.*, cb15574-Mu), PEP (Shanghai Yuanxin Biotech, *Co., Ltd.*, YX-160516M), ATP (Shanghai Yuanxin Biotech, *Co., Ltd.*, YX-W-A702), Asp (Shanghai Yuanxin Biotech, *Co., Ltd.*, YX-E29642), Malate (Shanghai Yuanxin Biotech, *Co., Ltd.*, YX-130109M), and GOT1 (Shanghai Yuanxin Biotech, *Co., Ltd.*, YX-071521M), Complex I (Shanghai Yuanxin Biotech, *Co., Ltd.*, YX-090000M), Complex III (Shanghai Yuanxin Biotech, *Co., Ltd.*, YX-090909M), Complex IV (Shanghai Yuanxin Biotech, *Co., Ltd.*, YX-092200M), Complex V (Shanghai Yuanxin Biotech, *Co., Ltd.*, YX-220000M), ROS (Shanghai Yuanxin Biotech, *Co., Ltd.*, YX-181519M), SOD (Shanghai Yuanxin Biotech, *Co., Ltd.*, YX-191504M).

Real-time quantitative PCR (RT-qPCR)

Total RNA was extracted from bone tissues and osteoblasts using TRIzol (Ambion, 15596026). Reverse transcription (RT-PCR) was carried out using Evo M-MLV RT Premix for qPCR (Accurate Biology, AG11706). RT-qPCR was performed using the SYBR Green Pro Taq HS qPCR kit (Accurate Biology, AG11701) according to the instruction manual. The reaction conditions were as follows: 95 °C for 2 min, 95 °C for 5 s for 25–30 cycles, and 60 °C for 30 s, with the collection of the fluorescence signal at the end of each cycle. A dissociation curve analysis was conducted for each RT-qPCR to confirm specific amplification products. The RT-qPCR primer sequences used are shown in Supplementary Table 2. All experiments were performed in duplicate and repeated three times. The relative target gene expression was normalized to β-actin using the $2^{-\Delta\Delta CT}$ method.

Untargeted metabolomics

The procedures were performed by Shanghai Bioprofile Technology Company Ltd. (Shanghai, China). All the procedures included sample collection, metabolite extraction, LC–MS detection, mass spectrometry data preprocessing, multivariate statistical analysis, differential metabolite identification and screening, and bioinformatics analysis. The metabolite was analyzed by HILIC in Agilent 1290 Infinity LC ultrahigh-performance liquid chromatography (UHPLC). Mass spectrometry analysis was performed on a Triple-TOF 5600 mass spectrometer (AB SCIEX). The raw MS data were processed using MS-DIAL for peak alignment, retention time correction, peak area extraction, and then compared with databases, which include public MS/MS libraries, such as MassBank, NIST14, ReSpect, and HMDB. The volcano plot was based on the standard of fold change (FC) > 1.5 or (FC) < 1/1.5 with a *P* value < 0.05. The significant differential metabolites were screened by (variable importance for the project) VIP > 1 with a *P* value < 0.05, clustered by hierarchical clustering, and then analyzed by the KEGG pathway using the KEGG database (http://www.kegg.jp). Enriched KEGG pathways were nominally statistically significant at the *P* < 0.05 level.

Targeted metabolomics

Targeted analyses of 200 metabolites and energy metabolites (including approximately 40 kinds of metabolites involved in the TCA cycle, glycolysis, oxidative phosphorylation, and pentose phosphate pathway) were performed by Shanghai Bioprofile Technology Company Ltd. (Shanghai, China).

Each bone sample was homogenized by a tissue crushing instrument, vortexed, ultrasonicated, and centrifuged to obtain the supernatant. Then, the supernatant was dried in a high-speed vacuum enrichment centrifuge. For mass spectrometry sampling analysis, the sample was redissolved in a 50% methanol solution and centrifuged at 20,000 g for 20 min at 4 °C, and the supernatant was obtained for analysis. The samples were separated by Shimadzu Nexera X2 LC-30AD high-performance liquid chromatography (HPLC). Mass spectrometry was performed using a QTRAP5500 Mass Spectrometer (AB SCIEX) in positive/negative ion mode. The original raw data of 200 metabolites, or energy metabolites, were processed by peak finding, alignment, and filtering using MultiQuant software. Metabolites with a fold change > 1.5 or fold change < 1/1.5 and *P* < 0.05 were considered significant.

Quantitative acetylome analysis

The procedures were performed by Shanghai Bioprofile Technology Company Ltd. (Shanghai, China). The samples were ground in liquid nitrogen and extracted with approximately 200 μl of SDT lysate. The extracted protein concentration was quantified with a BCA Protein Assay Kit (Nanjing Jiancheng Bioengineering Institute, W041-1-1). The quantified and analyzed proteins were enzymatically digested by trypsin into peptides. The peptides were subjected to acetylation enrichment by the PTMScan® Acetyl-Lysine Motif (Ac-K) Kit (Cell Signaling Technology, 13416). The peptides were then processed for LC–MS/MS analysis. Chromatographic separation was achieved on an EASY-nLC 1200 (Thermo Scientific). Mass spectrometric analysis was performed on a Q-Exactive HF-X mass spectrometer (Thermo Scientific). The mass spectrometric data
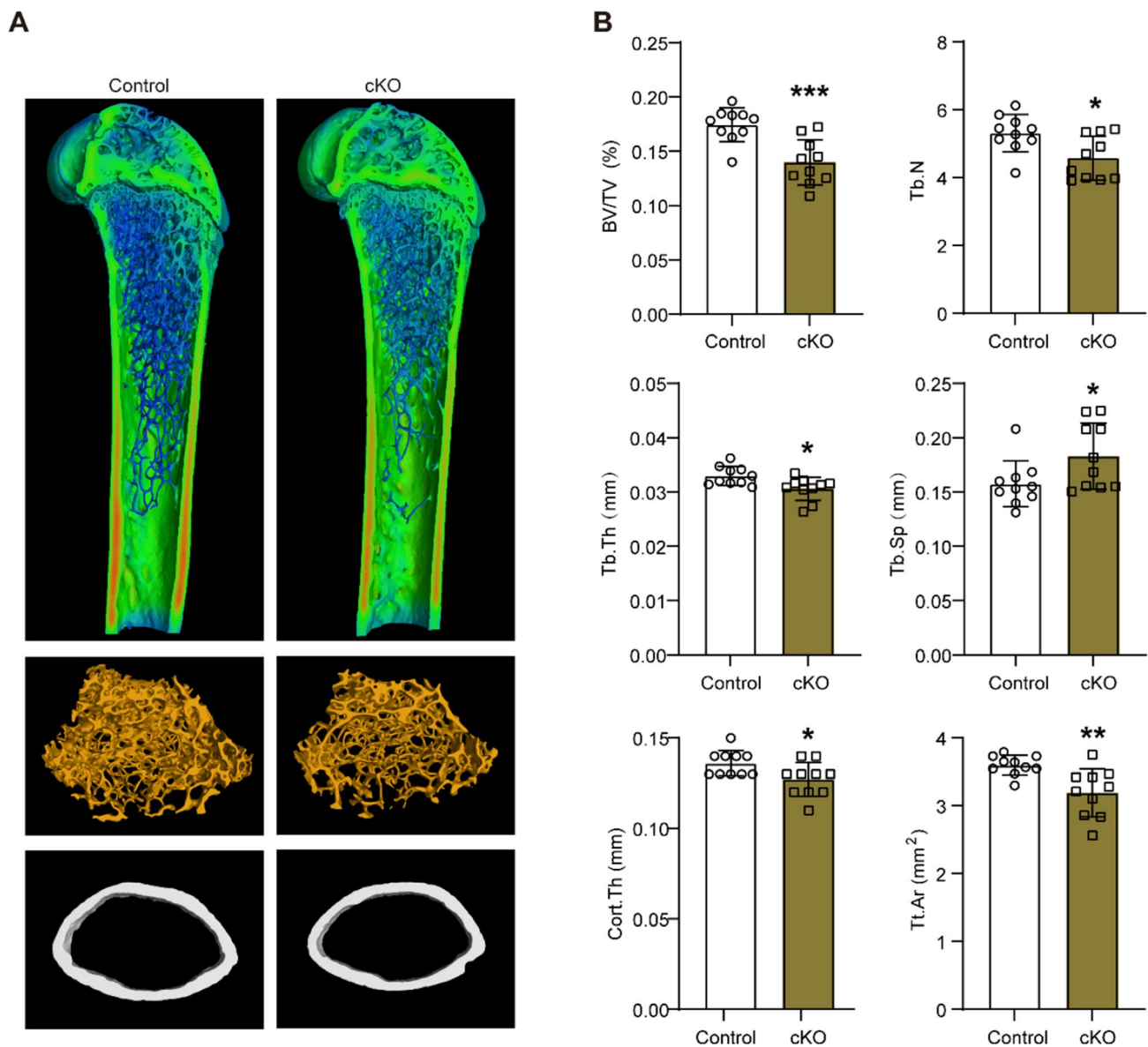
Fig. 1 *Sirt1* osteoblastic deletion inhibited bone mass. **A** Representative micro-CT images of femurs from control and cKO mice aged 8 weeks. **B** Quantification of the BV/TV, Tb.N, Tb.Th, Tb.Sp, Cort. Th, and Tt.Ar from the distal femur in control and cKO female mice aged 8 weeks ($n=10$/group). BV/TV: bone volume fraction; Tb.N: trabecular number; Tb.Th: trabecular thickness; Tb.Sp: trabecular separation; Cort.Th: cortical bone thickness; Tt.Ar: total cortical bone area. Data are presented as the mean $\pm$ SD, Student's t test; $*P<0.05$, $**P<0.01$, $***P<0.001$

were analyzed by MaxQuant 1.6.0.1.6 software against the protein database of UniProt-Mus musculus (mouse) [10090]-88108-210624. Carbamidomethylation on Cys was specified as a fixed modification, and oxidation on Met, acetylation on Lys, and acetylation on the protein N-terminus were specified as variable modifications. False discovery rate (FDR) thresholds for proteins, peptides, and modification sites were specified at 1%. The proteins whose acetylation sites significantly changed were identified as having a fold change (FC) > 1.5 or < 0.667 with a P value < 0.05. The modified sites' localization probability ≥ 0.75 was identified as high confidence.

Primary osteoblast and 3T3 E1 cells culture and treatment

Primary osteoblasts were extracted from neonatal calvariae with type II collagenase as previously described [33]. Osteoblastic 3T3E1 cells were purchased from Zhejiang Meisen Technology Co. Ltd. (Zhejiang, China). Calvaria cells of control and *Col1a-Cre/ERT2*; *Sirt1^flox/flox* mice and 3T3E1
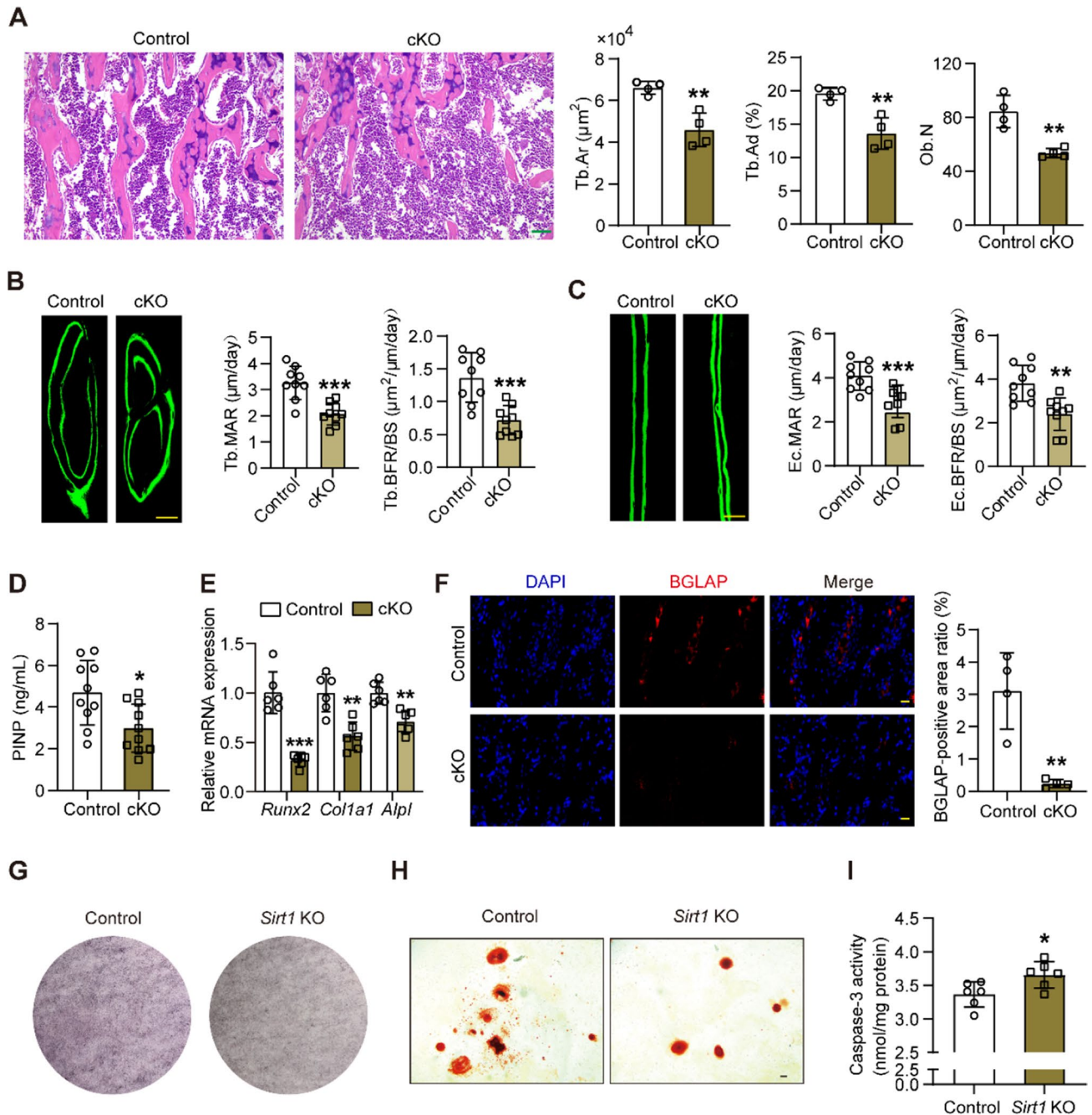
Fig. 2 Bone formation was decreased in cKO mice. **A** H&E staining of the bone structure in the distal femur sections of control and cKO mice aged 8 weeks. Bar = 50 μm. Right: quantification of Tb.Ar, Tb.Ad, and Ob.N in the distal femur sections of each group (n = 4/group). **B** Representative images of calcein double labeling in the distal femur sections of control and cKO mice aged 8 weeks. Bar = 100 μm. Right: quantification of Tb.MAR and Tb.BFR/BS in the distal femur sections of each group (n = 9/group). **C** Representative images of calcein double labeling in the distal femur sections of control and cKO mice aged 8 weeks. Bar = 100 μm. Right: quantification of Ec.MAR and Ec.BFR/BS in the distal femur sections of each group (n = 9/group). **D** ELISA analysis of serum PINP of control and cKO mice aged 8 weeks (n = 10/group). **E** Relative mRNA expression of *Runx2*, *Col1a1*, and *Alpl* in the femurs of control and cKO mice aged 8 weeks (n = 6/group). **F** Representative images of immunofluo-rescence staining of BGLAP (red) in distal femoral trabecular bone sections of control and cKO mice aged 8 weeks. The nucleus was stained blue. Bar = 20 μm. Right: quantification of BGLAP expression in distal femur sections of each group (n = 4/group). **G** Representative images of ALP staining of control and *Sirt1*KO osteoblasts. **H** Representative images of Alizarin Red S staining of control and *Sirt1*KO osteoblasts. Bar = 100 μm. **I** Quantification of Caspase-3 activity in control and *Sirt1*KO osteoblasts (n = 6/group). Tb.Ar: trabecular bone area, Tb.Ad: average distribution of trabecular bone, Ob.N: osteoblast number, Tb.MAR: trabecular bone mineralization apposition rate, Tb.BFR/BS: trabecular bone formation rate per bone surface, Ec.MAR: Endocortical bone mineralization apposition rate, Ec.BFR/BS: Endocortical bone formation rate per bone surface. Data are presented as the mean ± SD, Student's t test; *$P < 0.05$, **$P < 0.01$, ***$P < 0.001$

cells were cultured in α-modified modification medium (HyClone, SH30265.01) containing 1% penicillin/streptomycin (Gibco, 15140–122) and 10% foetal bovine serum (Gibco, 10270106). Osteoblast differentiation was induced with 50 µg/ml ascorbic acid (Solarbio, A8100), 10 mM β-glycerophosphate (Sigma, G5422), and 10 nM dexamethasone (Beyotime, ST1254). To induce *Sirt1* knockout, primary osteoblasts were treated with 1 µM 4-OH TM (Sigma, T176) for 7 days. Afterwards, 4-OH TM-treated primary osteoblasts isolated from *Col1a-Cre/ERT2*; *Sirt1^flox/flox* mice were designated *Sirt1*KO osteoblasts. For SIRT1 activity inhibition or activation, cells were treated with 10 µM EX-527 (Selleck, S1541) or 10 µM SRT2104 (Selleck, S7792) for 48 h.

Coculture of osteoclasts and primary osteoblasts

Murine bone marrow-derived macrophage cells were extracted and seeded in the transwell upper chamber, and differentiation was induced with α-modified modification medium containing 30 ng/ml M-CSF (Beyotime, P6015) and 100 ng/ml RANKL (MCE, HY-P73388) for 6–8 days to obtain osteoclasts as previously described [34]. Then, the osteoclast-seeded upper chamber was translocated to the receiver plate, where primary osteoblasts had been cultured in advance.

Osteoblast mineralization and apoptosis detection

Osteoblast mineralization detection was performed according to the procedures in the BCIP/NBT Alkaline Phosphatase (ALP) Color Development Kit (Beyotime, C3206) and the Alizarin Red S Staining Kit for Osteogenesis (Beyotime, C0148S). Osteoblast apoptosis analysis was performed according to the protocols in the Caspase 3 Activity Assay Kit (Beyotime, C1115).

Immunofluorescence staining and colocalization analysis

Primary osteoblasts at approximately 30–40% confluence were stained with anti-SIRT1 (1:50, Santa Cruz, sc-74465) and anti-GOT1 (1:50, Proteintech, 14886–1-AP) primary antibodies overnight at 4 °C, and then treated with secondary antibodies (1:200) at 37 °C for 1 h. The nuclei were stained with DAPI for 15 min. Colocalization analysis was performed using laser confocal microscopy (Leica, SP5 II).

Lentiviral plasmid information and transfection

Construction of the plasmids or lentiviruses was based on the gene *Sirt1* (Gene ID:93759) and *Got1* (Gene ID:14718). The wild-type SIRT1-HA, mutant SIRT1-H355A-HA,

wild-type GOT1-Flag, and mutant GOT1-K318R-Flag plasmids and lentiviruses were constructed by Genecarer Technology Company Ltd. (Shaanxi, China). CRISPR/Cas9 was applied to construct the recombinant vectors knocking out *Sirt1* and *Got1* gene (Genecarer, China). The *Sirt1* knockout and *Sirt1* overexpressing plasmids and lentiviruses were constructed by Shanghai Jikai Gene Chemical Technology Co. Ltd. The primers sequences used for plasmids construction were shown in Supplementary Table 3. The 3T3E1 cells were seeded in the 12-well plates and transfected with plasmids or infected with lentiviruses at 80% confluence. After 72 h, cells were treated with appropriate concentrations of puromycin. The puromycin-resistant cell pools were collected and identified by RT-qPCR or Western blotting.

Immunoprecipitation (IP) and western blotting

The cytoplasmic lysate was extracted according to the procedures using a Nuclear and Cytoplasmic Protein Extraction Kit (Beyotime, P0027). The extracted cytoplasmic lysate was incubated with the corresponding antibodies coupled to Protein A/G PLUS-Agarose (Santa Cruz, sc-2003) according to the manufacturer's instructions. The protein samples were extracted with RIPA lysis buffer (Beyotime, P0013B), separated by sodium dodecyl sulfate–polyacrylamide gel electrophoresis (SDS-PAGE) and transferred to polyvinylidene fluoride (PVDF) membranes. The PVDF membranes were then blocked with 5% milk and incubated with the primary antibody at 4 °C overnight. The next day, after incubation with the secondary antibody at 37 °C for 1 h, the specific protein bands were detected using an ECL detection substrate (Millipore, WBKLS0100). The following antibodies were used: acetyllysine (PTM BIO, PTM-105RM) (1:1000), crotonyllysine (PTM BIO, PTM-501) (1:1000), succinyllysine (PTM BIO, PTM-1419) (1:1000), SIRT1 (Abcam, ab189494) (1:1000), SIRT1 (FineTest, Fnab07877) (1:1000), GOT1(Proteintech, 12886-1-AP) (1:1000), GOT1 (Thermo Fisher, 14886-1-AP), β-actin (Proteintech, 66009-1-lg) (1:50,000), Flag (Proteintech, 66008-4-Ig), HA (Proteintech, 51064-2-AP), goat anti-rabbit IgG (Thermo, 31460) (1:10,000), goat anti-mouse IgG (Thermo, 31430) (1:10,000), goat anti-rabbit IgG (ZHUANGZHI, EK010) (1:10,000), and goat anti-mouse IgG (ZHUANG-ZHI, EK010) (1:10,000).

GOT1 activity inhibition

To inhibit the activity of GOT1, mice aged 8 weeks were treated with vehicle (saline) and/or 10 mg/kg aminooxyacetic acid (AOA) (MedChemExpress, HY-107994) every other day until dissection at 16 weeks, and osteoblasts were treated with vehicle or 100 µM AOA for 48 h.
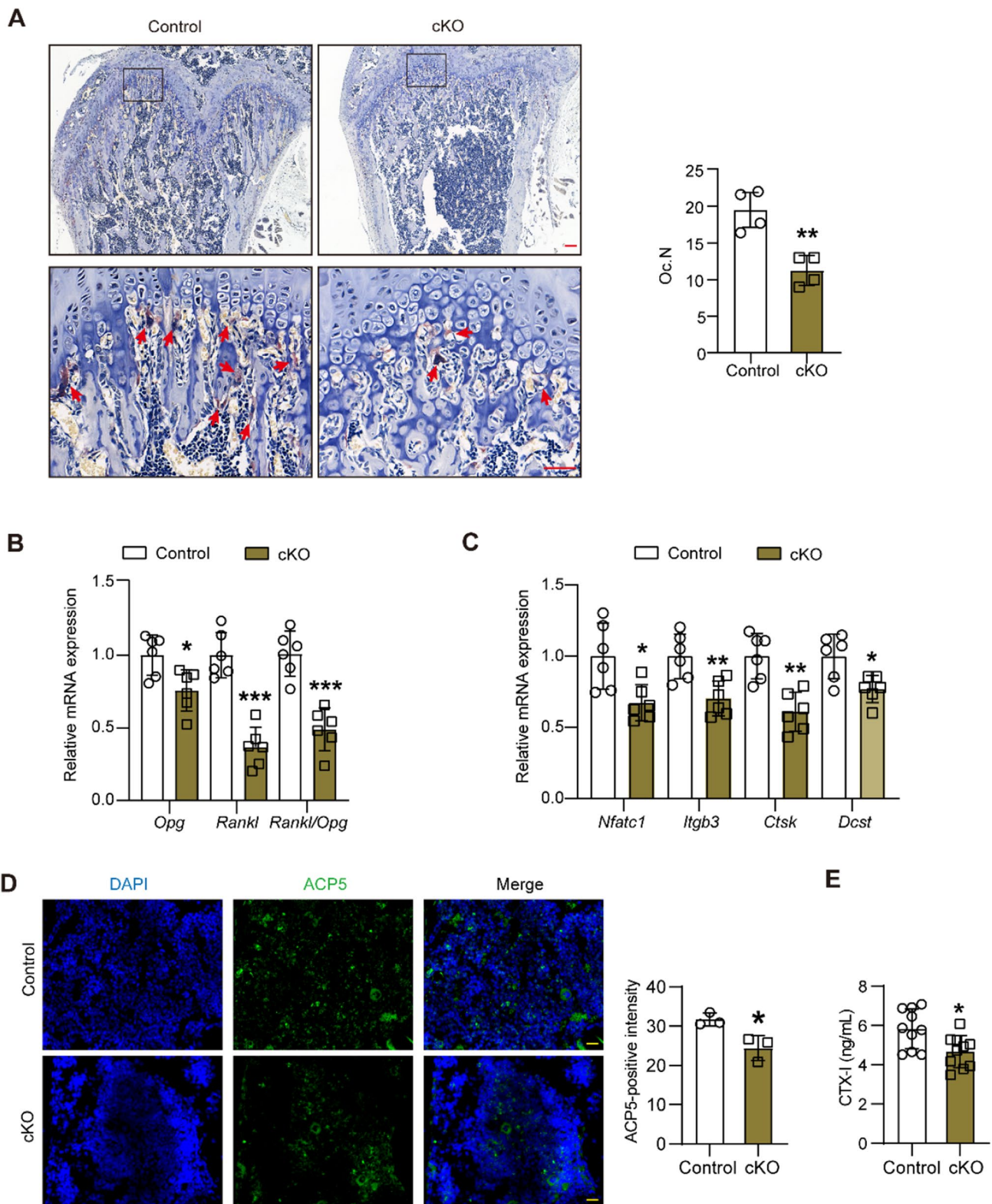
Statistics

Statistical analyses were performed using GraphPad Prism 9.0. For two groups, the normality of the data was tested using the D'Agostino-Pearson test, and the homogeneity of variance was tested using the F test. If the data were normally distributed with equal variance, they were analyzed using an unpaired two-tailed Student's t test; otherwise, they

◄**Fig. 3** Bone resorption was decreased in cKO mice. **A** Representative images of TRAP staining of osteoclasts (red arrows) in distal femur sections of control and cKO mice aged 8 weeks. Bar=100 μm and 50 μm. Right: quantification of the number of osteoclasts in the distal femur sections of each group (*n*=4/group). **B** Relative mRNA expression of *Opg*, *Rankl*, and *Rankl/ Opg* in control and cKO mice aged 8 weeks (*n*=6/group). **C** Relative mRNA expression of *Nfatc1*, *Itgb3*, *Ctsk*, and *Dcst* in control and cKO mice aged 8 weeks (*n*=6/group). **D** Representative images of immunofluorescence staining of ACP5 (green) in distal femoral trabecular bone sections of control and cKO mice aged 8 weeks. The nucleus was stained blue. Bar=100 μm. Right: quantification of ACP5 expression in distal femur sections of each group (*n*=3/group). **E** ELISA analysis of serum CTX-1 in control and cKO mice aged 8 weeks (*n*=10/group). Data are presented as the mean±SD, Student's *t* test; *$P<0.05$, **$P<0.01$, ***$P<0.001$

were analyzed using an unpaired two-tailed Student's *t* test with Welch's correction or a Mann–Whitney test. For more than two groups, significance was assessed using one-way ANOVA followed by Turkey Test. Differences were considered significant when the *P* value was <0.05. Data are expressed as the mean±SD.

Study approval

All procedures were performed in accordance with the recommendations in the NIH Guide for the Care and Use of Laboratory Animals. The Institutional Animal Ethics Committee of Xi'an Jiaotong University reviewed and approved the protocol.

Results

SIRT1 expression levels decreased with age in the bone tissue of mice

As SIRT1 expression levels have been reported to decrease with age [35], we thus tried to identify how SIRT1 expression changes with age in bone tissue. The bone mass throughout the lifespan in humans can be described as reaching the peak bone mass (PBM) in adulthood (~ 30 years old), and followed by a gradual decrease with aging in both genders [2]. We thus chose 24- and 48-week-old mice, which equally represent adult humans (~ 30 years old) that acquire peak bone mass and middle-aged mice (~ 45 years old) in which bone volume decreases, to observe the change in SIRT1 expression in mouse bone during aging. By double immunofluorescence staining of SIRT1 with COL1A1 in the distal femur, we found that SIRT1 protein expression levels in trabecular osteoblasts decreased in 48-week mice versus 24-week mice (Supplementary Fig. 1), indicating a pattern of decline in SIRT1 protein expression levels in osteoblasts with age.

Sirt1 osteoblastic deficiency inhibited trabecular and cortical bone mass

To precisely address the role of SIRT1 in osteoblastic lineage cells, we used TM-inducible *Sirt1* conditional knockout (cKO) mice (Supplementary Fig. 2A). Cre recombinase enzyme was activated in the osteoblasts upon TM incubation, as demonstrated by *Col1a-Cre/ERT2; Sirt1$^{-/-}$; Rosa26-LSL-Tdtomato* mice, which expressed tomato in the osteoblastic lineage cells (Supplementary Fig. 2B), and *Col1a-Cre/ERT2; Sirt1$^{-/-}$; ROSA26-mTmG* mice, which expressed EGFP, replaced tomato in the cell membrane of the osteoblastic lineage cells (Supplementary Fig. 2C). *Sirt1* was specifically deleted in the calvaria and femur of cKO mice but not in other tissues (heart, liver, spleen, lung, kidney) (Supplementary Fig. 2D). *Sirt1* mRNA levels were decreased by 60% in the femurs of cKO mice, as demonstrated by RT-qPCR (Supplementary Fig. 2E). Accordingly, SIRT1 protein expression was downregulated in the femurs of cKO mice, as detected by western blotting and immunohistochemistry (Supplementary Fig. 2F, G). Collectively, these results demonstrate that *Sirt1* is specifically deleted in osteoblasts by using Col1a-Cre/ERT2 mice.

Micro-CT analysis of the femurs revealed that *Sirt1* osteoblastic knockdown led to a decrease in both trabecular and cortical bone mass (Fig. 1). Eight-week-old female cKO mice femurs showed a decrease in bone volume per tissue volume (BV/TV), trabecular number (Tb.N), and trabecular thickness (Tb.Th), and an increase in trabecular separation (Tb.Sp) (Fig. 1B). Meanwhile, the cortical thickness (Ct.Th) and total cortical area (Tt.Ar) significantly decreased in the femurs of cKO mice aged 8 weeks (Fig. 1A, B). The 16-week-old female cKO mice had similar phenotypes (Supplementary Fig. 3). All the results indicate that *Sirt1* osteoblastic knockdown inhibited bone mass.

Sirt1 deficiency inhibited bone formation

Consistent with the lower bone mass analyzed by micro-CT, H&E staining analysis results indicated that the cKO mice had lower trabecular bone area (Tb.Ar), average distribution of trabecular bone (Tb.Ad), and trabecular osteoblast number (Tb.N) of the distal femur (Fig. 2A). Calcein green double staining analysis also confirmed that the mineral apposition rate (MAR) and bone formation rate per bone surface (BFR/BS) were decreased in both the trabecular and cortical bone of cKO mice (Fig. 2B, C). The serum levels of procollagen I N-terminal propeptide (PINP), a biomarker of bone formation, were reduced in cKO mice (Fig. 2D). The mRNA and protein levels of osteoblast differentiation markers, including *Runx2*, collagen1 α1(*Col1a1*), alkaline phosphatase
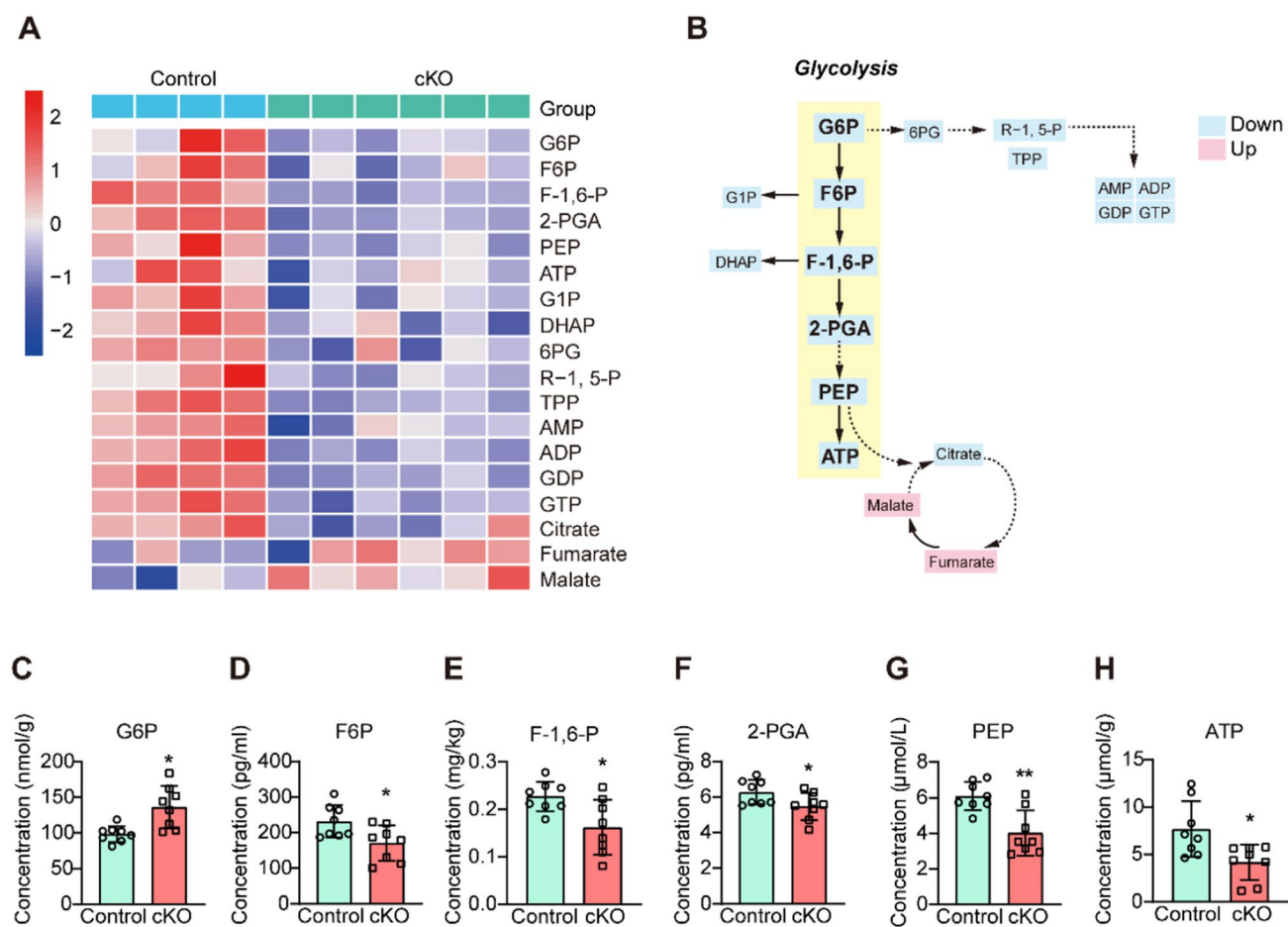
Fig. 4 *Sirt1* deletion affected bone metabolism in cKO mice. **A** Heatmap of the metabolism in the femurs between control and cKO mice aged 8 weeks by targeted energy metabolism. **B** Summary diagram of changes in energy metabolites in cKO group versus control group. Blue background indicates the downregulated metabolite, pink background indicates the upregulated metabolite. **C–H** Quantitative concentrations of the metabolites involved in core glycolysis of femurs between control and cKO groups by ELISA kits ($n=8$/group). Data are presented as the mean $\pm$ SD, Student's t test; *$P < 0.05$, **$P < 0.01$, ***$P < 0.001$

(*Alpl)*, and bone gamma carboxyglutamate protein (*Bglap),* were decreased in the femurs of cKO mice (Fig. 2E, F). The effects of *Sirt1* deletion on osteoblasts were examined. The gene expression levels of osteoblast differentiation markers were also decreased in *Sirt1*KO osteoblasts (Supplementary Fig. 4A, B). The mineralization was inhibited in *Sirt1*KO osteoblasts, as demonstrated by ALP and Alizarin Red S staining (Fig. 2G, H). Furthermore, the apoptosis of osteoblasts was increased in *Sirt1*KO osteoblasts (Fig. 2I). All the above results indicate that *Sirt1* deficiency inhibited osteoblast differentiation and mineralization, increased osteoblast apoptosis, and as a result, inhibited bone formation.

Sirt1 deficiency inhibited bone resorption

As bone homeostasis is regulated by both bone formation and bone resorption, we further investigated bone resorption upon *Sirt1* knockdown. TRAP staining analysis indicated

that osteoclast numbers decreased in the femur trabecular bone of cKO mice (Fig. 3A). Gene expression levels of *Rankl*, *Opg*, and *Rankl/Opg*, released by osteoblasts to regulate the activity of osteoclasts, were downregulated in cKO mice and *Sirt1*KO osteoblasts (Fig. 3B and Supplementary Fig. 4C). The gene expression levels of nuclear factor of activated T cells, cytoplasmic, calcineurin-dependent 1 (*Nfatc1*), integrin beta 3 (*Itgb3*), cathepsin K (*Ctsk*), and DC-STAMP domain-containing 1 (*Dcst)* were downregulated in the femurs of cKO mice, as well as in osteoclasts that were cocultured in transwell chambers with *Sirt1*KO osteoblasts (Fig. 3C and Supplementary Fig. 4D). The protein expression level of acid phosphatase 5, tartrate resistant (ACP5) was also decreased in the femur cancellous bone of cKO mice (Fig. 3D). Moreover, serum level of C-terminal telopeptide of type-1 collagen (CTX-1), a biomarker of bone resorption, was decreased in cKO mice (Fig. 3E). Thus, the inhibited bone resorption in cKO mice was a causable effect

of inhibited bone formation. Altogether, the lower bone mass in cKO mice was a balance of inhibited bone formation and bone resorption.

Sirt1 knockdown inhibited glycolysis of osteoblasts

SIRT1 has been reported to regulate metabolism. As such, we next investigated how SIRT1 regulates osteoblastic metabolism by using targeted energy metabolomics to detect 40 kinds of common energy metabolites. Hierarchical clustering showed the relationship of the metabolites between the femurs of the two groups (Fig. 4A). Metabolite enrichment analysis indicated that SIRT1 deletion significantly changed the levels of metabolites involved in glycolysis, purine metabolism, and the Tricarboxylic acid (TCA) cycle (Fig. 4A, B). The levels of metabolites involved in glycolysis were decreased in the cKO mice, including glucose-6-phosphate (G6P), fructose-6-biphosphate (F6P), fructose-1,6-biphosphate (F-1,6-P), 2-phosphoglycerate (2-PGA), phosphoenolpyruvate (PEP), adenosine triphosphate (ATP), glucose-1-phosphate (G1P), dihydroxyacetone phosphate (DHAP), 6-phosphogluconate (6PG), ribose 5-phosphate (R-1,5-P), and thiamine pyrophosphate (TPP) (Fig. 4A, B). In purine metabolism, the levels of metabolites were decreased in the cKO mice, including adenosine monophosphate (AMP), adenosine diphosphate (ADP), guanosine diphosphate (GDP), and guanosine triphosphate (GTP) (Fig. 4A, B). In the TCA cycle metabolites, the levels of citrate decreased, whereas the levels of malate and fumarate increased in the cKO group (Fig. 4A, B). Overall, the above results indicated that *Sirt1* deletion changed the relative levels of intermediates in the core glycolysis pathway (G6P, F6P, F-1,6-P, 2-PGA, PEP, and ATP), its side pathway (G1P and DHAP), another side pathway of the pentose phosphate pathway (PPP) (6PG, R-1,5-P, and TPP), and PPP-derived purine metabolism (AMP, ADP, GDP, and GTP), as well as downstream of the TCA cycle (citrate, fumarate, and malate) (Fig. 4A, B). Glycolysis is a main energy source for osteoblasts [18, 20, 21, 36, 37], and SIRT1 has been reported to regulate glycolysis [23–25, 38]. Thus, it is reasonable to assume that the changes in all metabolites upon *Sirt1* knockdown resulted from changes in the core glycolysis pathway. Therefore, we aimed to verify the levels of metabolites in the core glycolysis pathway in control and cKO mice. Indeed, the levels of G6P, F6P, F-1,6-P, 2-PGA, PEP, and ATP were decreased in cKO mice, as demonstrated by ELISA kits (Fig. 4C–H). These results indicated that glycolysis was decreased in osteoblasts of cKO mice.

Based on the above results, we further tried to detect whether *Sirt1* inhibition regulates other metabolic pathways using untargeted metabolism and targeted metabolomics, P200 (200 kinds of metabolites) (Supplementary Figs. 5, 6). Differential analysis indicated that *Sirt1* loss significantly

changed the abundance of intermediates in purine and pyrimidine metabolism, consistent with the results in energy metabolism (Supplementary Figs. 5, 6). Purine and pyrimidine metabolism were all derived from PPP, the side pathway of core glycolysis. Therefore, these results further confirmed that *Sirt1* knockdown inhibited glycolysis in bone.

Sirt1 knockdown affected protein lysine acetylation levels in bone

SIRT1 has been reported to function by regulating acylation [39]. Thus, to investigate the acylation levels of proteins under *Sirt1* osteoblastic knockdown, three types of lysine acetylation were detected by Western blotting in femur lysates of control and cKO mice (Fig. 5A). SIRT1 mainly functioned through deacetylation of the protein lysine residues in osteoblasts, as demonstrated by a marked elevation in lysine acetylation; however, there was little elevation in lysine crotonylation and succinylation in the cKO group versus the control group (Fig. 5A). Then we tested which protein was the potential deacetylation target of SIRT1 in osteoblasts. We performed a quantitative acetylome analysis and identified a total of 10,233 lysine acetylation (Kac) sites (918 in the control group and 945 in the cKO group) and 512 proteins (487 in the control group and 494 in the cKO group) in the femurs of both groups (Fig. 5B, C). Among the identified proteins, 71 proteins exhibited significant changes in Kac sites, 39 proteins were upregulated in Kac sites, and 37 proteins were downregulated in Kac sites of the cKO group versus the control group, as some proteins themselves have different Kac sites (Fig. 5C and Supplementary Fig. 7A). All the identified Kac site-changed proteins (KSCP) in the cKO group versus the control group were mainly localized in the cytoplasm, membrane, and mitochondrion (Supplementary Fig. 7B). Hierarchical analysis of the KSCP demonstrated a moderate distinction between the two groups (Fig. 5D). To further detect the functions of these KSCP, GO annotation and KEGG pathway enrichment analyses were performed (Supplementary Fig. 7C–F). Interestingly, consistent with the KEGG pathway analysis, the Wiki pathway analysis also indicated that KSCP were enriched in energy metabolism, including the glycolysis and gluconeogenesis, oxidative phosphorylation, and TCA cycle (Fig. 5E).

As the femur is formed by endochondral ossification, in addition to osteoblasts, it includes various kinds of cells, such as osteoclasts, chondrocytes, and adipocytes. The calvaria are formed by intramembranous bone formation, i.e., the cells directly differentiated into osteoblasts, and hence it consisted of most osteoblastic lineages. As such, to exclude the potential impacts of other kinds of cells on osteoblasts in the femur, we also conducted quantitative acetylome analysis of the calvaria (Fig. 5F–I and Supplementary Fig. 8). A total of 665 acetylation sites (546 in the control group and 633 in
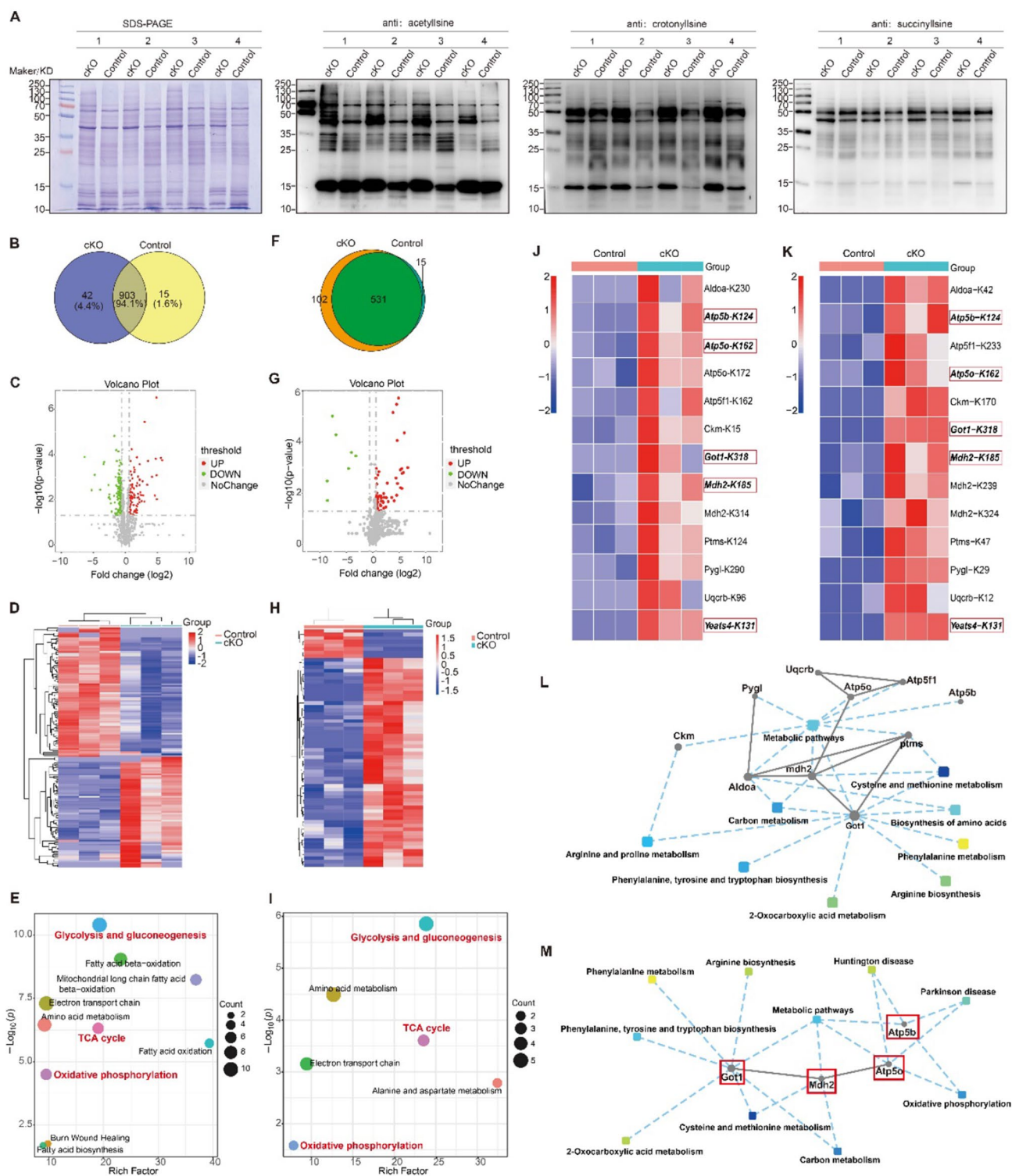
the cKO group) and 903 proteins (894 in the control group and 710 in the cKO group) were identified in both groups (Fig. 5F, G). Among the identified proteins, 156 proteins had reliable Kac sites, 31 proteins exhibited significant changes in Kac sites, 26 proteins were upregulated in Kac sites, and 7 proteins were downregulated in Kac sites of the cKO group

versus the control group, as some proteins themselves had different Kac sites (Fig. 5G and Supplementary Fig. 8A). All the KSCP were also mainly localized in the cytoplasm, membrane, and mitochondrion (Supplementary Fig. 8B). Hierarchical analysis of the KSCP demonstrated a moderate distinction between the two groups (Fig. 5H). GO annotation

◀**Fig. 5** *Sirt1* deletion affected the acetylation sites of the proteins in both the femur and calvaria of mice aged 8 weeks. **A** Western blotting analysis of femurs from control and cKO mice by acetyllsine, crotonyllsine, and succinyllsine antibodies. **B** Venn diagram of the acetylation sites detected from the femurs between control and cKO mice. **C** Volcano plot of the distribution of the total reliable proteins in Kac sites in the femurs between control and cKO mice. **D** Hierarchical clustering of differentially expressed proteins in Kac sites in the femurs between control and cKO mice. **E** Wiki pathway analysis of differentially expressed proteins in Kac sites in the femurs between control and cKO mice. **F** Venn diagram of the acetylation sites detected from the calvaria between control and cKO mice. **G** Volcano plot of the distribution of the total reliable proteins in Kac sites in the calvaria between control and cKO mice. **H** Hierarchical clustering of differentially expressed proteins in Kac sites in the calvaria between control and cKO mice. **I** Wiki pathway analysis of differentially expressed proteins in Kac sites in the calvaria between control and cKO mice. **J** Heatmap of proteins in which the acetylation sites upregulated in the femurs of the cKO mice versus the control mice. **K** Heatmap of proteins in which the acetylation sites upregulated in the calvaria of the cKO mice versus the control mice. **L** Protein–protein interaction network of the same proteins with the acetylation sites upregulation in both the femurs and calvaria of the cKO mice versus the control mice. **M** Protein–protein interaction network of the same proteins with the same acetylation sites upregulation in both the femurs and calvaria of the cKO mice versus the control mice

enrichment analyses were performed to detect the functions of these KSCP (Supplementary Fig. 8C–E). Interestingly, the KEGG pathway and Wiki pathway analyses also indicated that KSCP were enriched in energy metabolism, including the glycolysis and gluconeogenesis, oxidative phosphorylation, and TCA cycle (Fig. 5I and Supplementary Fig. 8F).

To identify the direct target proteins of SIRT1 deacetylation, we cross-analyzed the KSCP in both femurs and calvaria. Analysis indicated that 11 kinds of proteins whose Kac site levels were upregulated were coexpressed, which further confirmed the reliability of the quantitative acetylome analysis results (Fig. 5J, K). Protein–protein network analysis also indicated that these proteins were closely associated (Fig. 5L). We further cross-analyzed the proteins with the same Kac site upregulation in both the femurs and calvaria of the cKO mice versus the control mice. Analysis indicated that 5 proteins with the same Kac site upregulation in the cKO mice versus the control mice were coexpressed in both the femurs and calvaria, including Got1, Mdh2, Atp5o, Atp5b, and Yeast4 (Fig. 5J, K). Among the 5 proteins, the K124 site in Atp5b, K162 site in Atp5o, K318 site in Got1, K185 site in Mdh2, and K131 site in Yeats4 were significantly upregulated in the cKO group versus the control group, both in the femur and calvaria (Fig. 5J, K). Protein–protein network analysis indicated that 4 (Got1, Mdh2, Atp5o, and Atp5b) of the 5 proteins were closely related and coinvolved in metabolic pathways (Fig. 5M). Thus, we focused on the 4 proteins with acetylation site upregulation as potential SIRT1 direct target proteins in osteoblasts.

SIRT1 inhibited GOT1 enzyme activity by catalyzing its lysine deacetylation

SIRT1 was found to be mainly localized in the nucleus and cytoplasm. Among the above identified 4 kinds of Kac site upregulated proteins (Got1, Mdh2, Atp5o, and Atp5b), Mdh2, Atp5o, and Atp5b were found to be mainly localized in mitochondria, and only Got1 was subcellularly localized in the cytoplasm. Our study demonstrated that *Sirt1* deletion inhibits glycolysis, and GOT1 is also a glycolytic protein [40, 41]. Therefore, GOT1 may be the potential substrate that directly interacts with SIRT1 to regulate glycolysis in osteoblasts. GOT1 has been reported to play vital roles in the Asp-malate shuttle [27]. Interestingly, the inhibited Asp level and increased malate level in femur of cKO mice reflect that GOT1 activity was activated upon *Sirt1* knockdown (Fig. 6A, B). In addition, ELISA analysis showed that GOT1 enzyme activity was higher in the femurs of cKO mice (Fig. 6C). These results suggest that *Sirt1* knockdown activated GOT1 enzyme activity. As such, we hypothesized that SIRT1 may physiologically interact with GOT1 and deacetylate GOT1, thus regulating GOT1 activity in osteoblasts.

Indeed, immunofluorescence staining indicated that SIRT1 and GOT1 colocalized in osteoblasts (Fig. 6D). GOT1 had Kac sites, and upon *Sirt1* knockout or overexpression, the protein level of GOT1 showed no change, but the Kac level of GOT1 was upregulated or downregulated (Fig. 6E). Furthermore, the upregulated Kac level of GOT1 upon *Sirt1* knockout was rescued by *Sirt1* overexpression (Fig. 6F). These results imply that SIRT1 interacts with GOT1 to regulate the Kac level of GOT1 in osteoblasts. To verify whether SIRT1 regulates GOT1 by its deacetylation function, we further used SRT2104 (a SIRT1 activity activator) or EX-527 (a SIRT1 activity inhibitor) to treat osteoblastic 3T3E1 cells and found that the protein level of GOT1 had no change, but the Kac level of GOT1 was decreased or increased accordingly (Fig. 6G). Moreover, the catalytically inactive mutant deacetylase-inactive SIRT1-H355A failed to induce the deacetylation of GOT1 compared with wild-type SIRT1 (Fig. 6H). Collectively, these results indicated that SIRT1 interacted with GOT1 and deacetylated GOT1 in osteoblasts.

As screened by quantitative acetylome analysis, Kac site 318 in GOT1 was higher upon *Sirt1* knockdown (Fig. 5J, K). To verify whether the K318 site was deacetylated by SIRT1, we performed site-directed mutagenesis. One mutant GOT1 was generated, in which the lysine (K) 318 residues were substituted with arginine (R). The wild-type GOT1 plasmids and K318R mutant plasmids were transfected into control and *Sirt1* knockout osteoblastic 3T3E1 cells. As a result, the K318R mutation leads to a decrease in the acetylation of GOT1 (Fig. 6I). Furthermore, *Sirt1* knockout significantly increased the acetylation level of wild-type GOT1 but not
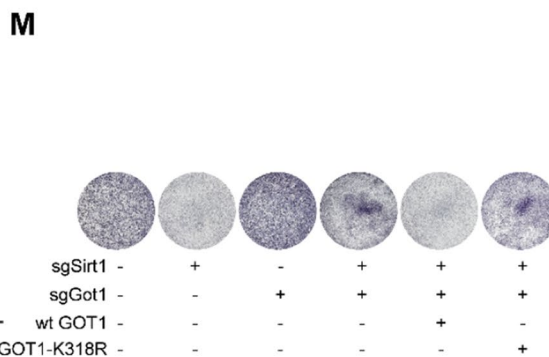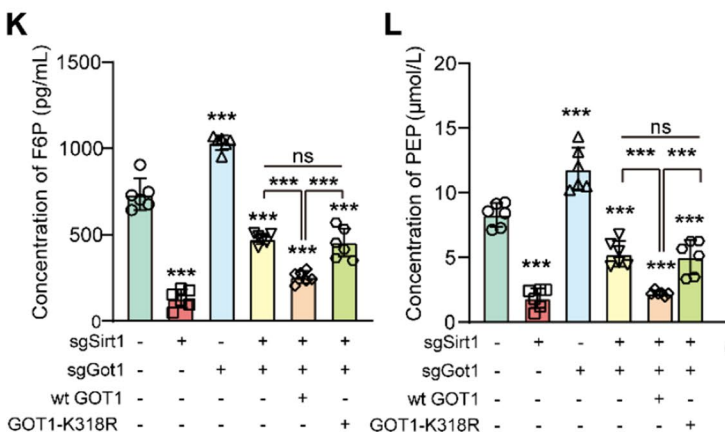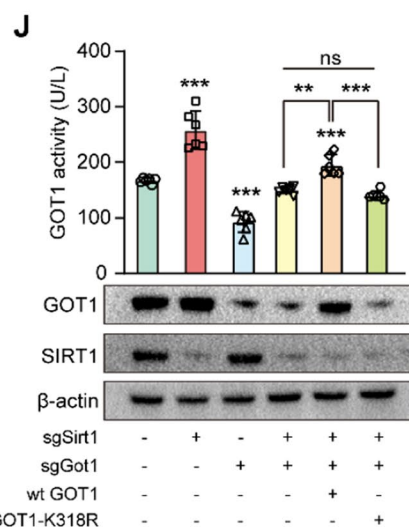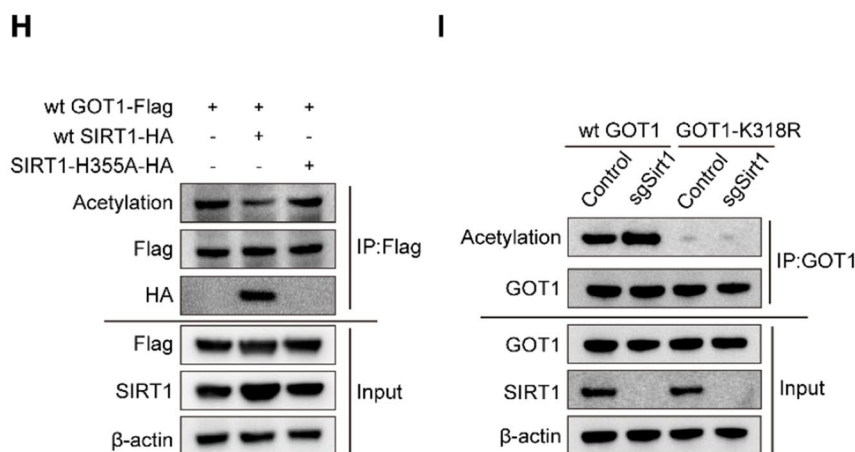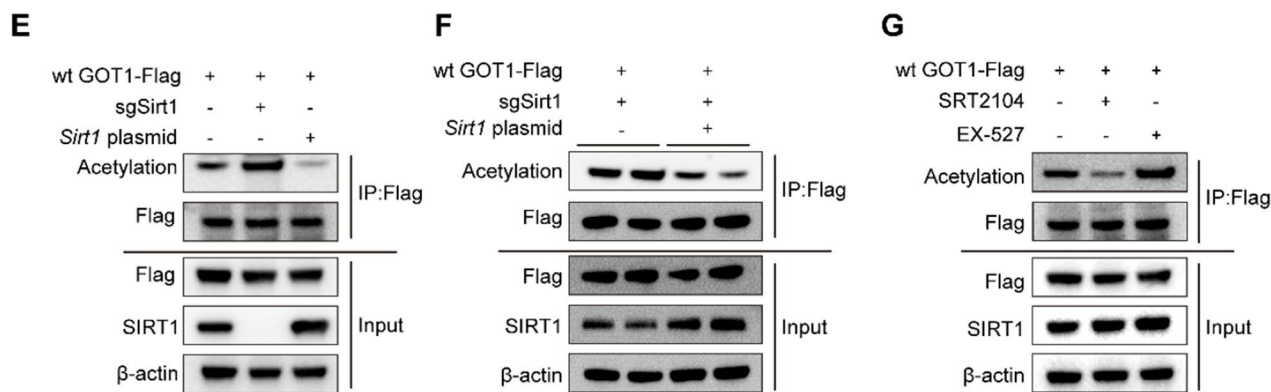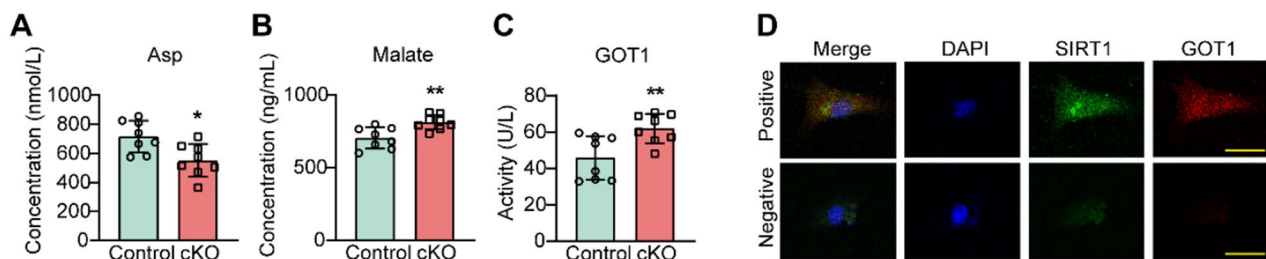
◀**Fig. 6** SIRT1 inhibited GOT1 enzyme activity by catalyzing its lysine deacetylation. **A** The concentration of Asp in the femurs of the control and cKO mice aged 8 weeks measured by an ELISA Kit ($n=8$/group). **B** The concentration of malate in the femurs of the control and cKO mice aged 8 weeks measured by an ELISA Kit ($n=8$/group). **C** The activity of GOT1 in the femurs of the control and cKO mice aged 8 weeks measured by an ELISA Kit ($n=8$/group). **D** The subcellular localization of SIRT1 and GOT1 in primary osteoblasts. **E** The protein level and Kac level of GOT1 upon *Sirt1* deletion or overexpression in 3T3E1 cells. **F** The Kac level of GOT1 in *Sirt1* knockout 3T3E1 cells upon *Sirt1* overexpression. **G** The Kac level of GOT1 in 3T3E1 cells treated with SRT2104 or EX-527. **H** The Kac level of GOT1 protein immunoprecipitated from 3T3E1 cells transfected with SIRT1 plasmids or mutant SIRT1-H355A plasmids. **I** Control and *Sirt1* knockout 3T3E1 cells were transfected with Wild-type GOT1 or GOT1-K318R mutant plasmids. The Kac level of GOT1 protein immunoprecipitated from the above cells. **J** *Sirt1*-knockout/*Got1*- knockout 3T3E1 cells were transfected with Wild-type GOT1 or GOT1-K318R mutant plasmids. The GOT1 activity was measured in the above cells. **K** *Sirt1*-knockout/*Got1*- knockout 3T3E1 cells were transfected with Wild-type GOT1 or GOT1-K318R mutant plasmids. The levels of F6P in glycolysis were measured in the above cells. **L** *Sirt1*-knockout/*Got1*- knockout 3T3E1 cells were transfected with Wild-type GOT1 or GOT1-K318R mutant plasmids. The levels of PEP in glycolysis were measured in the above cells. **M** *Sirt1*-knockout/*Got1*- knockout 3T3E1 cells were infected with Wild-type GOT1 or GOT1-K318R mutant virus. The ALP staining of osteoblast mineralization was conducted in the above cells. Data are presented as the mean ± SD, Student's *t* test (a, b, c); one-way ANOVA with Tukey's test (j, k, l), *$P<0.05$, **$P<0.01$, ***$P<0.001$

that of the GOT1-K318R mutant (Fig. 6I). These data suggest that lysine 318 in GOT1 proteins is the primary deacetylation target of SIRT1.

To further identify the function of GOT1-318R acetylation under *Sirt1* deletion, *Got1-*/*Sirt1*-double knockout cells were generated by CRISPR/Cas9 technique. The above cells were then transfected with wild-type GOT1 or GOT1-K318R mutant plasmids (Fig. 6J). *Got1* knockout abolished *Sirt1*-knockout-mediated increase of GOT1 enzymatic activity, while re-expression of wild-type GOT1 but not GOT1-K318R restored this activity (Fig. 6J). Thus, K318R deacetylation by SIRT1 is primarily responsible for SIRT1-mediated abrogation of GOT1 activity in osteoblasts. *Got1* knockout inhibited the effects of *Sirt1*-knockout on the levels of F6P and PEP in glycolysis, while re-expression of wild-type GOT1 rescued them (Fig. 6K, L). However, re-expression of GOT1-K318R failed to restore these metabolite levels in *Got1-*/*Sirt1*-double knockout osteoblasts (Fig. 6K, L). We also found that re-expression of wild-type *Got1* could rescue the osteoblastic mineralization in *Got1-*/*Sirt1*-double knockout osteoblasts, whereas re-expression of GOT1-K318R was unable to rescue these functions (Fig. 6M). These results indicate that SIRT1 inhibits GOT1 enzymatic activity by deacetylating GOT1 at lysine 318, which leads to the effect on glycolysis and osteoblast function.

SIRT1 regulated osteoblast glycolysis via GOT1

We further inhibited the function of GOT1 by GOT1 inhibitor aminooxyacetate (AOA) treatment in cKO mice, to observe whether GOT1 inhibition had an effect on glycolysis (Fig. 7A). The ELISA results, the higher Asp expression level, and the lower malate expression level indicate that GOT1 activity was inhibited in AOA-treated cKO mice (Fig. 7B–D). Upon AOA treatment, the femoral bone mass was significantly reversed in cKO mice, including the BV/TV, Tb.N, and Tb.Sp (Fig. 7E, F). Interestingly, the metabolism levels in the glycolysis pathway, including G6P, F6P, F-1,6-P, 2-PGA, PEP, and ATP, were significantly increased upon AOA treatment in cKO mice (Fig. 7G). These results indicate that GOT1 regulates glycolysis upon *Sirt1* knockdown in osteoblasts. We also analyzed osteoblast function and found that AOA treatment reversed the differentiation, mineralization, and apoptosis of osteoblasts (Fig. 7H–K). Altogether, these results indicate that SIRT1 deacetylates GOT1 to regulate glycolysis, thus affecting the function of osteoblasts and bone mass (Fig. 8).

Discussion

In this study, we demonstrated the role of *Sirt1* during bone modeling and remodeling and found the followings: (1) Physiologically, the protein expression levels of SIRT1 in osteoblasts of femoral bone decreased with aging. (2) Postnatal loss of *Sirt1* in osteoblasts decreased trabecular and cortical bone mass. (3) SIRT1 regulated bone metabolism by intervening in osteoblast glycolysis through deacetylation of GOT1.

Emerging studies have demonstrated that SIRT1 has antiaging protective roles [5], and its expression at the transcription and protein levels decreased with aging in mammalian tissues, such as brain, liver, skeletal muscle, and white adipose tissues [35, 42, 43]. Recently, conflicting data have been reported regarding the expression of SIRT1 in bone tissues. One study showed that the mRNA expression of SIRT1 was significantly downregulated in mice aged 16 months compared with young mice aged 2 months [12]. In contrast, other studies indicated that the mRNA expression of SIRT1 was not different between 3-month-old mice, 12-month-old mice, and 24-month-old mice [14, 44]. These contrary results may be accounted for by the different bone tissues (calvaria versus. long bone) isolated from the mice. In addition, the internal reference genes used for relative quantification of *Sirt1* expression were different, among which *Gapdh* gene expression was reported to downregulate with age [45]. To clarify the pattern of SIRT1 expression in bone tissues, we used in situ fluorescence labeling to localize the expression of SIRT1. We found that the SIRT1
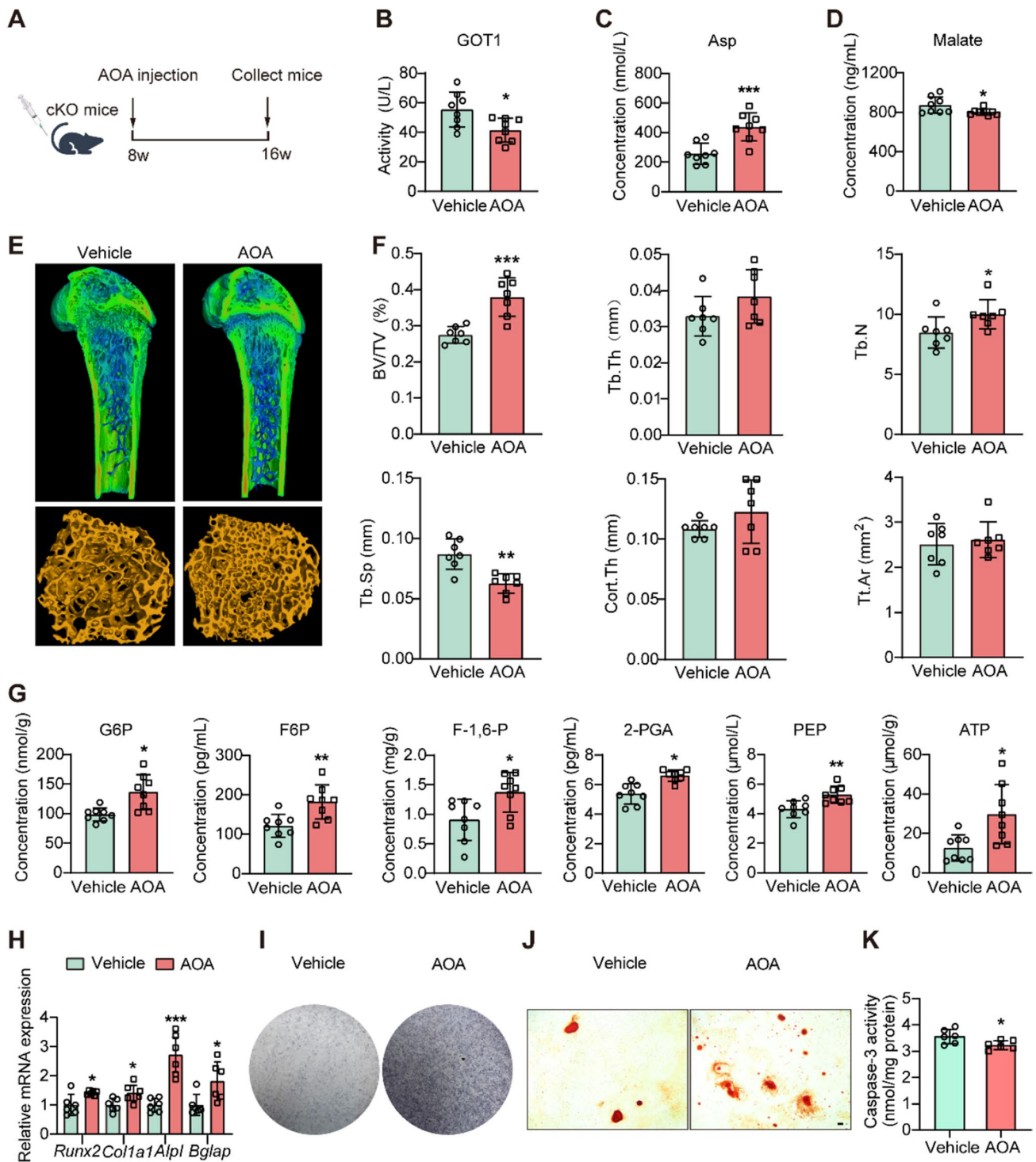
protein was expressed in osteoblasts of trabecular bone, and its expression level decreased with aging, implicating the involvement of *Sirt1* in skeletal homeostasis throughout life.

The bone mass phenotypes of *Col1a-cre/ERT2*; *Sirt1⁻/⁻* mice in our present study were similar to those of other osteoblastic lineage-specific *Sirt1*-knocdown mice,

including *Prdx1-Cre*; *Sirt1⁻/⁻*, *Osx-Cre*; *Sirt1⁻/⁻*, and *Col1a1-Cre*; *Sirt1⁻/⁻* transgenic mice [11–14].

The lower bone mass is caused by either decreased bone formation or increased bone resorption (osteoporosis) [4]. In the transgenic mice of *Prdx1-Cre*; *Sirt1⁻/⁻*, *Osx-Cre*; *Sirt1⁻/⁻*, and *Col1a1-Cre*; *Sirt1⁻/⁻*, where the *Sirt1* was specifically deleted at different differentiation stages

◀**Fig. 7** SIRT1 affected the acetylation level of GOT1 and glycolysis to regulate bone mass. **A** Schematic of experimental design. The 8-week cKO mice treated with vehicle or AOA until dissection at 16 weeks. **B** GOT1 activity of 16-week cKO mice treated with vehicle or AOA ($n = 8$/group). **C** The concentration of Asp in 16-week cKO mice treated with vehicle or AOA ($n = 8$/group). **D** The concentration of malate in 16-week cKO mice treated with vehicle or AOA ($n = 8$/group). **E** Representative micro-CT images of the femurs in 16-week cKO mice treated with vehicle or AOA. **F** Quantification of the BV/TV, Tb.N, Tb.Th, and Tb.Sp from the distal femurs in 16-week cKO mice treated with vehicle or AOA ($n = 7$/group). **G** Quantification of the metabolites in glycolysis after AOA treatment in 16-week cKO mice ($n = 8$/group). **H** Relative mRNA expression of *Runx2*, *Col1a1*, *Alpl*, and *Bglap* in *Sirt1*KO osteoblasts treated with vehicle or AOA ($n = 6$/group). **I** Representative images of ALP staining of *Sirt1*KO osteoblasts treated with vehicle or AOA. **J** Representative images of Alizarin Red S staining of *Sirt1*KO osteoblasts treated with vehicle or AOA. **K** Quantification of caspase-3 activity in *Sirt1*KO osteoblasts treated with vehicle or AOA ($n = 6$/group). BV/TV: bone volume fraction; Tb.Th: trabecular thickness; Tb.N: trabecular number; Tb.Sp: trabecular separation; Cort.Th: cortical bone thickness; Tt.Ar: total cortical bone area. Data are presented as the mean ± SD, Student's t test; $*P < 0.05$, $**P < 0.01$, $***P < 0.001$

of osteoblastic lineage, the lower bone mass was mainly caused by decreased bone formation [11–14]. However, in our study of *Col1a-cre/ERT2*; *Sirt1$^{-/-}$* mice, the reduced overall bone mass was balanced by inhibited bone formation and bone resorption, with the former exceeding the latter to some extent. The *Col1a-cre/ERT2*; *Sirt1$^{-/-}$* mice exhibited a decrease in trabecular and cortical bone mass, including BV/TV, Tb.N, Tb.Th, Tb.Sp, Cort.Th, and Tt.Ar. Remarkably, the decrease in both trabecular and cortical bone mass was consistent with the decreases in the Tb.MAR, Tb.BFR/BS, Ec.MAR, Ec.BFR/BS, Tb.Ar, and Tb.Ad of cKO mice. Furthermore, osteoblast functions were inhibited upon *Sirt1* knockdown, as determined by the decreased osteoblast number and activity. The decrease in osteoblast activity was reflected by the decrease in osteoblast differentiation and mineralization and the increase in osteoblast apoptosis. Therefore, overall bone formation decreased dramatically, as indicated by the decreased serum PINP level. In addition, the expression level of *Rankl*/*Opg*, a signal released by osteoblasts to regulate the activity of osteoclasts, was significantly reduced. And the osteoclast number and enzyme activity decreased. Moreover, the expression level of CTX-1, a serum bone resorption marker, significantly decreased. These results led to the inhibition of bone resorption in our study. Recently, the induced abundance of H-type vessels, which supply osteoblast and osteoclast with oxygen and nutrient to activate their activities, have been demonstrated to inhibit bone loss of osteoporosis [46, 47]. As the result of *Sirt1*-osteoblastic ablation, less abundant H-type vessels were observed in our cKO mice (data not shown), which has further confirmed the inhibited osteoblastic and osteoclastic function. In conclusion, the lower bone mass in our present study was mainly due to the decreased bone formation upon *Sirt1*-deletion, companied with inhibited bone resorption.

Although the bone mass phenotypes of *Col1a-cre/ERT2*; *Sirt1$^{-/-}$ mice* in our study were consistent with the other two studies of *Col1a1-Cre*; *Sirt1$^{-/-}$* mice [12, 14], the *Sirt1* knockdown window was different, utilizing two different Cre recombination transgenic mice (i.e., *Col1a-cre/ERT2* versus *Col1a1-Cre*). The *Col1a1* gene is expressed early in the embryo when osteoblasts begin to differentiate [48, 49]. Therefore, *Sirt1* inactivation occurred in the embryonic stage upon the expression of the *Col1a1* gene, thus impacting bone growth, modeling, and remodeling in *Col1a1-Cre*; *Sirt1$^{-/-}$* mice [12, 14]. Consequently, the lower bone mass was a result of the cumulative effect, starting from embryogenesis and continuing to adulthood, in the adult 16-week *Col1a1-Cre*; *Sirt1$^{-/-}$ mice* [12, 14]. This observation can also explain why the decreased bone mass was age dependent, only observed in 16-week *Col1a1-Cre*; *Sirt1$^{-/-}$* mice, instead of 4-week *Col1a1-Cre*; *Sirt1$^{-/-}$* mice [12, 14]. In contrast, *Sirt1* was deleted after birth in *Col1a-cre/ERT2*; *Sirt1$^{-/-}$ mice* in our study, when embryonic development was completed, upon inducible Cre recombinase activation after intraperitoneal TM administration [32]. Adolescence is the key period throughout the life cycle for the accrual of PBM [2]. Therefore, using *Col1a-cre/ERT2* transgenic mice allows us to study the function of *Sirt1* deletion on bone mass postnatally, which accumulates from birth to adolescence and is then sustained into adulthood, excluding the embryonic stages.

Glycolysis was inactive upon *Sirt1* knockdown in our study. With the development of technology, various omics technologies have been applied to explore the pathogenesis of bone-related diseases [49]. However, none of these technologies alone could fully elucidate the disease's pathological features and therefore cannot comprehensively dissect the underlying molecular and signaling mechanisms in vivo [50]. Metabolomics is one kind of omics technology that can amplify smaller changes at the protein level which cannot be detected by other omics technologies [50]. In present study, untargeted and targeted metabolomics approaches were used to detect the levels of metabolites upon *Sirt1* knockdown. Glycolysis is the main metabolic pathway to meet ATP demand during osteoblast differentiation for osteoblast-mediated bone formation [18, 19, 51]. Although SIRT1 has been reported to be a regulator of glycolysis [23–26], whether SIRT1 regulates glycolysis in osteoblasts was still unclear. In present study, upon *Sirt1* knockdown, the levels of metabolism in glycolysis, including G6P, F6P, F-1,6-P, 2-PGA, PEP, and ATP, were significantly decreased, as detected by targeted metabolomics and further verified by the corresponding ELISA kits.
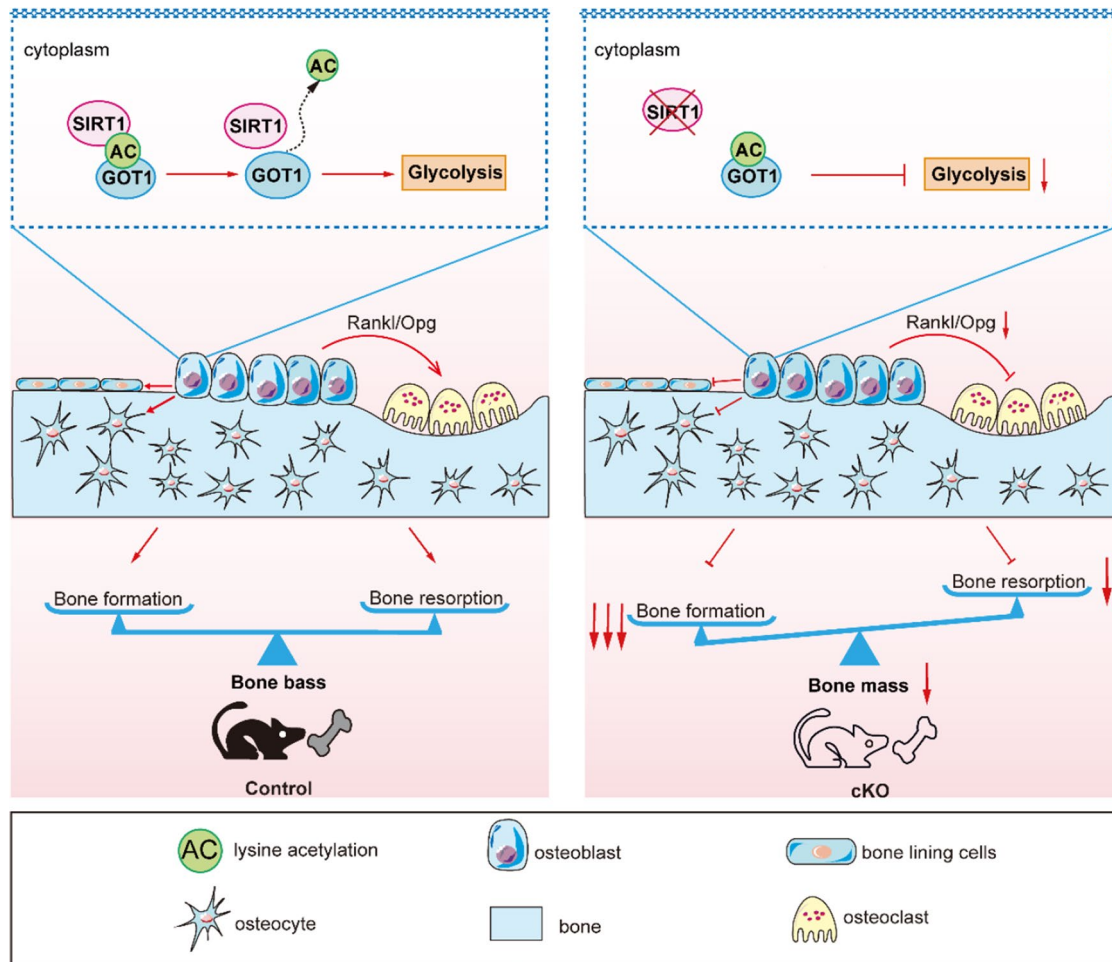
Fig. 8 Schematic diagram of SIRT1 deacetylating GOT1 to regulate glycolysis in osteoblasts. SIRT1 deletion induced acetylation of GOT1, thereby inhibited the process of glycolysis to decrease bone formation by osteoblasts. The decreased bone formation then inhibited bone resorption. Thus, bone mass decreased

Current study identified GOT1 as a deacetylation target of SIRT1 in osteoblasts that regulates bone mass. SIRT1 has been reported to function by regulating the acetylation [39] and crotonylation [52] levels of protein lysine residues. Lysine acetylation/deacetylation, one of the most extensively studied protein posttranslational modifications (PTMs), is involved in key cellular processes relevant to physiology and disease, such as protein stability, protein subcellular localization, enzyme activity, and protein–protein interactions [39]. In this study, SIRT1 was shown to mainly function as a deacetylase in osteoblasts. Emerging evidence from *Sirt1* osteoblastic knockout animal models reported that SIRT1 affected the activity of the transcription factors (FOXOs and NF-KB) and transcription co-factors (β-catenin, in the Wnt-pathway), the very targets of SIRT1 deacetylase function in osteoblasts, thus protecting bone mass [11–14]. However, the mechanism by which SIRT1 deacetylates in osteoblasts to regulate bone homeostasis is not fully understood. GOT1, a cytosolic enzyme, reversibly

catalyzes the Asp-malate shuttle [27]. GOT1 also plays vital roles in glutamine metabolism, and hence, it has become a new therapeutic target for the development of anticancer agents [27]. A very recent study demonstrated that targeting glutamine metabolism may improve skeletal stem cells in aging and enhance osteoblast differentiation, as well as its activity to increase bone mass [53]. This report implies that GOT1 may have an impact on osteoblasts. In pancreatic ductal adenocarcinoma, lysine 369 of GOT1 was deacetylated by SIRT5, another family member of sirtuins, to enhance glutathione metabolism, indicating that the acetylation level of GOT1 played vital roles in cell metabolic processes [54]. Remarkably, our present study showed that *Sirt1* knockdown increased the acetylation level of GOT1 in osteoblasts, as screened by quantitative acetylome analysis in both the femur and calvaria. Furthermore, we found that GOT1 activity was activated in cKO mice, as demonstrated by the lower Asp level and higher malate level, as well as the ELISA results. Moreover, IP and site-mutation experiments

demonstrated that lysine 318 of GOT1 was deacetylated by SIRT1 in osteoblasts. Upon treatment with the GOT1 inhibitor AOA, bone mass was significantly rescued in cKO mice, further verifying the interaction of SIRT1 and GOT1 in osteoblasts in regulating bone mass.

We discovered that GOT1 inhibited glycolysis upon *Sirt1* deletion to regulate bone mass. In addition to its role in the Asp-malate shuttle and glutamate and α-KG conversion, GOT1 has also been reported to be associated with glycolysis in various cancers and other diseases [28, 30, 40, 41, 55]. Oncomine cancer database analysis found GOT1 to be one of the 11 key glycolytic proteins that were upregulated in breast cancer patients with a poor prognosis [55]. GOT1 expression level was upregulated in pancreatic cancer tissues and cell lines [56], and *Got1* inhibition uniquely disrupted the glycolysis pathway [41] in pancreatic ductal adenocarcinoma cells. Inhibition of *Got1* also induced glucose consumption and lactate secretion rates in the cancer cell lines 143B and A549 [40]. Moreover, in oesophageal squamous cancer cells, *Got1* inhibition induced cell proliferation, migration, aerobic glycolysis, and glycolysis-mediated cisplatin resistance [30]. In addition to its role in cancer cells, GOT1 regulation of glycolysis also played vital roles in other diseases and cellular processes. In aging and diabetes, *Got1* knockout increased glycolysis, disordered beta-cell function, and impaired cellular identity [28]. Another recent study also indicated that GOT1 promoted the glycolytic programming of cytotoxic T lymphocytes [29]. These results suggested that GOT1 regulated glycolysis. In our study of cKO mice, GOT1 activity was activated; however, glycolysis was inhibited, implying that GOT1 activity was negatively correlated with glycolysis. Furthermore, upon *Got1* inhibition, the reduced glycolysis level was partially rescued in cKO mice, as evidenced by the glycolysis metabolites, including G6P, F6P, F-1,6-P, 2-PGA, PEP, and ATP. Meanwhile, bone mass and osteoblast functions were rescued. These rescued results suggested that *Sirt1* regulates glycolysis, at least in part, through GOT1 in osteoblasts.

SIRT1 is a well-known metabolic sensor that plays a vital role in metabolism, including glucose metabolism. Our study revealed that SIRT1 deacetylates GOT1 to regulate glycolysis and affect the homeostasis of mitochondrial function in osteoblast. The latter was demonstrated by decreases in respiratory chain complex activity and SOD concentration, and an increase in ROS concentration upon *Sirt1* deletion (Supplementary Fig. 9). Consistent with our findings, the study by Somemura S. et al. reported that an increase in glucose uptake of osteoblasts, induced by mechanic loading, weakened SIRT1 activity, and eventually interfered with cellular energy metabolism [57].

Altogether, we conclude that removal of *Sirt1* in osteoblast caused bone loss by disruption of bone formation coupled with inhibition of bone resorption, which resulted from inhibition of osteoblast glycolysis through inducing the lysine acetylation of GOT1 in osteoblasts.

Declarations

Conflict of interest The authors have no any conflict to declare.

Consent for publication All authors have agreed for publication.

Ethical approval There are no human samples used in this study.

References

1. Karsenty G, Khosla S (2022) The crosstalk between bone remodeling and energy metabolism: a translational perspective. Cell Metab 34(6):805–817. https://doi.org/10.1016/j.cmet.2022.04.010
2. Zhu X, Zheng H (2021) Factors influencing peak bone mass gain. Front Med 15(1):53–69. https://doi.org/10.1007/s11684-020-0748-y
3. Almeida M, Laurent MR, Dubois V, Claessens F, O'Brien CA, Bouillon R, Vanderschueren D, Manolagas SC (2017) Estrogens and androgens in skeletal physiology and pathophysiology. Physiol Rev 97(1):135–187. https://doi.org/10.1152/physrev.00033.2015
4. Gao Y, Patil S, Jia J (2021) The development of molecular biology of osteoporosis. Int J Mol Sci 22(15):8182. https://doi.org/10.3390/ijms22158182
5. Bonkowski MS, Sinclair DA (2016) Slowing ageing by design: the rise of NAD(+) and sirtuin-activating compounds. Nat Rev Mol Cell Biol 17(11):679–690. https://doi.org/10.1038/nrm.2016.93
6. Wu QJ, Zhang TN, Chen HH, Yu XF, Lv JL, Liu YY, Liu YS, Zheng G, Zhao JQ, Wei YF et al (2022) The sirtuin family in health and disease. Signal Transduct Target Ther 7(1):402. https://doi.org/10.1038/s41392-022-01257-8

7. Gertz M, Steegborn C (2016) Using mitochondrial sirtuins as drug targets: disease implications and available compounds. Cell Mol Life Sci 73(15):2871–2896. https://doi.org/10.1007/s00018-016-2180-7

8. Wang AJ, Zhang J, Xiao M, Wang S, Wang BJ, Guo Y, Tang Y, Gu J (2021) Molecular mechanisms of doxorubicin-induced cardiotoxicity: novel roles of sirtuin 1-mediated signaling pathways. Cell Mol Life Sci 78(7):3105–3125. https://doi.org/10.1007/s00018-020-03729-y

9. Li Q, Cheng JC, Jiang Q, Lee WY (2021) Role of sirtuins in bone biology: potential implications for novel therapeutic strategies for osteoporosis. Aging Cell 20(2):e13301. https://doi.org/10.1111/acel.13301

10. Zainabadi K (2019) Drugs targeting SIRT1, a new generation of therapeutics for osteoporosis and other bone related disorders? Pharmacol Res 143:97–105. https://doi.org/10.1016/j.phrs.2019.03.007

11. Simic P, Zainabadi K, Bell E, Sykes DB, Saez B, Lotinun S, Baron R, Scadden D, Schipani E, Guarente L (2013) SIRT1 regulates differentiation of mesenchymal stem cells by deacetylating beta-catenin. EMBO Mol Med 5(3):430–440. https://doi.org/10.1002/emmm.201201606

12. Edwards JR, Perrien DS, Fleming N, Nyman JS, Ono K, Connelly L, Moore MM, Lwin ST, Yull FE, Mundy GR et al (2013) Silent information regulator (Sir)T1 inhibits NF-B signaling to maintain normal skeletal remodeling. J Bone Miner Res 28(4):960–969. https://doi.org/10.1002/jbmr.1824

13. Iyer S, Han L, Bartell SM, Kim HN, Gubrij I, de Cabo R, O'Brien CA, Manolagas SC, Almeida M (2014) Sirtuin1 (Sirt1) promotes cortical bone formation by preventing beta-catenin sequestration by FoxO transcription factors in osteoblast progenitors. J Biol Chem 289(35):24069–24078. https://doi.org/10.1074/jbc.M114.561803

14. Zainabadi K, Liu CJ, Caldwell ALM, Guarente L (2017) SIRT1 is a positive regulator of in vivo bone mass and a therapeutic target for osteoporosis. PLoS ONE 12(9):e0185236. https://doi.org/10.1371/journal.pone.0185236

15. Cohen-Kfir E, Artsi H, Levin A, Abramowitz E, Bajayo A, Gurt I, Zhong L, D'Urso A, Toiber D, Mostoslavsky R et al (2011) Sirt1 is a regulator of bone mass and a repressor of Sost encoding for sclerostin, a bone formation inhibitor. Endocrinology 152(12):4514–4524. https://doi.org/10.1210/en.2011-1128

16. Gu X, Wang Z, Gao J, Han D, Zhang L, Chen P, Luo G, Han B (2019) SIRT1 suppresses p53-dependent apoptosis by modulation of p21 in osteoblast-like MC3T3-E1 cells exposedto fluoride. Toxicol In Vitro 57:28–38. https://doi.org/10.1016/j.tiv.2019.02.006

17. Yao H, Yao Z, Zhang S, Zhang W, Zhou W (2018) Upregulation of SIRT1 inhibits H_2O_2-induced osteoblast apoptosis via FoxO1/beta-catenin pathway. Mol Med Rep 17(5):6681–6690. https://doi.org/10.3892/mmr.2018.8657

18. Lee WC, Guntur AR, Long F, Rosen CJ (2017) Energy metabolism of the osteoblast: implications for osteoporosis. Endocr Rev 38(3):255–266. https://doi.org/10.1210/er.2017-00064

19. van Gastel N, Carmeliet G (2021) Metabolic regulation of skeletal cell fate and function in physiology and disease. Nat Metab 3(1):11–20. https://doi.org/10.1038/s42255-020-00321-3

20. Motyl KJ, Guntur AR, Carvalho AL, Rosen CJ (2017) Energy metabolism of bone. Toxicol Pathol 45(7):887–893. https://doi.org/10.1177/0192623317737065

21. Guntur AR, Gerencser AA, Le PT, DeMambro VE, Bornstein SA, Mookerjee SA, Maridas DE, Clemmons DE, Brand MD, Rosen CJ (2018) Osteoblast-like MC3T3-E1 cells prefer glycolysis for ATP production but adipocyte-like 3T3-L1 cells prefer oxidative phosphorylation. J Bone Miner Res 33(6):1052–1065. https://doi.org/10.1002/jbmr.3390

22. Peck WA, Birge SJ Jr, Fedak SA (1964) Bone cells: biochemical and biological studies after enzymatic isolation. Science 146(3650):1476–1477. https://doi.org/10.1126/science.146.3650.1476

23. Chen YT, Yang H, Chen SY, Lu ZH, Li BX, Jiang TK, Xuan M, Ye RF, Liang HR, Liu XS et al (2022) SIRT1 regulated hexokinase-2 promoting glycolysis is involved in hydroquinone-enhanced malignant progression in human lymphoblastoid TK6 cells. Ecotoxicol Environ Saf 241:113757. https://doi.org/10.1016/j.ecoenv.2022.113757

24. Liu G, Bi Y, Shen B, Yang H, Zhang Y, Wang X, Liu H, Lu Y, Liao J, Chen X et al (2014) SIRT1 limits the function and fate of myeloid-derived suppressor cells in tumors by orchestrating HIF-1alpha-dependent glycolysis. Cancer Res 74(3):727–737. https://doi.org/10.1158/0008-5472.CAN-13-2584

25. Lv Q, Wang K, Qiao SM, Yang L, Xin YR, Dai Y, Wei ZF (2018) Norisoboldine, a natural AhR agonist, promotes Treg differentiation and attenuates colitis via targeting glycolysis and subsequent NAD(+)/SIRT1/SUV39H1/H3K9me3 signaling pathway. Cell Death Dis 9(3):258. https://doi.org/10.1038/s41419-018-0297-3

26. Rodgers JT, Lerin C, Haas W, Gygi SP, Spiegelman BM, Puigserver P (2005) Nutrient control of glucose homeostasis through a complex of PGC-1 alpha and SIRT1. Nature 434(7029):113–118. https://doi.org/10.1038/nature03354

27. Song ZR, Yang YY, Wu YL, Zheng MZ, Sun DJ, Li H, Chen LX (2022) Glutamic oxaloacetic transaminase 1 as a potential target in human cancer. Eur J Pharmacol 917:174754. https://doi.org/10.1016/j.ejphar.2022.174754

28. Murao N, Yokoi N, Takahashi H, Hayami T, Minami Y, Seino S (2022) Increased glycolysis affects beta-cell function and identity in aging and diabetes. Mol Metab 55:101414. https://doi.org/10.1016/j.molmet.2021.101414

29. Xu W, Patel CH, Zhao L, Sun IH, Oh MH, Sun IM, Helms RS, Wen JY, Powell JD (2023) GOT1 regulates CD8+effector and memory T cell generation. Cell Rep 42(1):111987. https://doi.org/10.1016/j.celrep.2022.111987

30. Zhou S, Guo Z, Lv X, Zhang X (2022) CircGOT1 promotes cell proliferation, mobility, andglycolysis-mediated cisplatin resistance via inhibiting its host gene GOT1 in esophageal squamous cell cancer. Cell Cycle 21(3):247–260. https://doi.org/10.1080/15384101.2021.2015671

31. Li H, Rajendran GK, Liu N, Ware C, Rubin BP, Gu Y (2007) SirT1 modulates the estrogen-insulin-like growth factor-1 signaling for postnatal development of mammary gland in mice. Breast Cancer Res 9(1):R1. https://doi.org/10.1186/bcr1632

32. Kim JE, Nakashima K, de Crombrugghe B (2004) Transgenic mice expressing a ligand-inducible Cre recombinase in osteoblasts and odontoblasts: a new tool to examine physiology and disease of postnatal bone and tooth. Am J Pathol 165(6):1875–1882. https://doi.org/10.1016/S0002-9440(10)63240-3

33. Li H, Li D, Ma Z, Qian Z, Kang X, Jin X, Li F, Wang X, Chen Q, Sun H et al (2018) Defective autophagy in osteoblasts induces endoplasmic reticulum stress and causes remarkable bone loss. Autophagy 14(10):1726–1741. https://doi.org/10.1080/15548627.2018.1483807

34. Zhang J, Zhao L, Wang N, Li J, He F, Li X, Wu S (2019) Unexpected role of matrix Gla protein in osteoclasts: inhibiting osteoclast differentiation and bone resorption. Mol Cell Biol 39(12):e00012-19. https://doi.org/10.1128/MCB.00012-19

35. Chen C, Zhou M, Ge Y, Wang X (2020) SIRT1 and aging related signaling pathways. Mech Ageing Dev 187:111215. https://doi.org/10.1016/j.mad.2020.111215

36. Jin ZX, Kho J, Dawson B, Jiang MM, Chen YQ, Ali S, Burrage LC, Grover M, Palmer DJ, Turner DL et al (2021) Nitric oxide modulates bone anabolism through regulation of osteoblast

glycolysis and differentiation. J Clin Investig 131(5):e138935. https://doi.org/10.1172/JCI138935

37. Song F, Lee WD, Marmo T, Ji X, Song C, Liao X, Seeley R, Yao L, Liu H, Long F (2023) Osteoblast-intrinsic defect in glucose metabolism impairs bone formation in type II diabetic male mice. Elife 12:e85714. https://doi.org/10.7554/eLife.85714

38. Koronowski KB, Khoury N, Saul I, Loris ZB, Cohan CH, Stradecki-Cohan HM, Dave KR, Young JI, Perez-Pinzon MA (2017) Neuronal SIRT1 (silent information regulator 2 homologue 1) regulates glycolysis and mediates resveratrol-induced ischemic tolerance. Stroke 48(11):3117–3125. https://doi.org/10.1161/STROKEAHA.117.018562

39. Shang S, Liu J, Hua F (2022) Protein acylation: mechanisms, biological functions and therapeutic targets. Signal Transduct Target Ther 7(1):396. https://doi.org/10.1038/s41392-022-01245-y

40. Zhou X, Curbo S, Li F, Krishnan S, Karlsson A (2018) Inhibition of glutamate oxaloacetatetransaminase 1 in cancer cell lines results in altered metabolism with increased dependency of glucose. BMC Cancer 18(1):559. https://doi.org/10.1186/s12885-018-4443-1

41. Nelson BS, Lin L, Kremer DM, Sousa CM, Cotta-Ramusino C, Myers A, Ramos J, Gao T, Kovalenko I, Wilder-Romans K et al (2020) Tissue of origin dictates GOT1 dependence and confers synthetic lethality to radiotherapy. Cancer Metab 8:1. https://doi.org/10.1186/s40170-019-0202-2

42. Cho SH, Chen JA, Sayed F, Ward ME, Gao F, Nguyen TA, Krabbe G, Sohn PD, Lo I, Minami S et al (2015) SIRT1 deficiency in microglia contributes to cognitive decline in aging and neurodegeneration via epigenetic regulation of IL-1beta. J Neurosci 35(2):807–818. https://doi.org/10.1523/JNEUROSCI.2939-14.2015

43. Gong H, Pang J, Han Y, Dai Y, Dai D, Cai J, Zhang TM (2014) Age-dependent tissue expression patterns of Sirt1 in senescence-accelerated mice. Mol Med Rep 10(6):3296–3302. https://doi.org/10.3892/mmr.2014.2648

44. Fukuda M, Yoshizawa T, Karim MF, Sobuz SU, Korogi W, Kobayasi D, Okanishi H, Tasaki M, Ono K, Sawa T et al (2018) SIRT7 has a critical role in bone formation by regulating lysine acylation of SP7/Osterix. Nat Commun 9(1):2833. https://doi.org/10.1038/s41467-018-05187-4

45. Calvi LM, Sims NA, Hunzelman JL, Knight MC, Giovannetti A, Saxton JM, Kronenberg HM, Baron R, Schipani E (2001) Activated parathyroid hormone/parathyroid hormone-related protein receptor in osteoblastic cells differentially affects cortical and trabecular bone. J Clin Invest 107(3):277–286. https://doi.org/10.1172/JCI11296

46. Peng Y, Wu S, Li Y, Crane JL (2020) Type H blood vessels in bone modeling and remodeling. Theranostics 10(1):426–436. https://doi.org/10.7150/thno.34126

47. Kusumbe AP, Ramasamy SK, Adams RH (2014) Coupling of angiogenesis and osteogenesis by a specific vessel subtype in bone. Nature 507(7492):323–328. https://doi.org/10.1038/nature13145

48. Dacquin R, Starbuck M, Schinke T, Karsenty G (2002) Mouse alpha 1(I)-collagen promoter is the best known promoter to drive efficient Cre recombinase expression in osteoblast. Dev Dyn 224(2):245–251. https://doi.org/10.1002/dvdy.10100

49. Liu F, Woitge HW, Braut A, Kronenberg MS, Lichtler AC, Mina M, Kream BE (2004) Expression and activity of osteoblast-targeted Cre recombinase transgenes in murine skeletal tissues. Int J Dev Biol 48(7):645–653. https://doi.org/10.1387/ijdb.041816fl

50. Yang TL, Shen H, Liu A, Dong SS, Zhang L, Deng FY, Zhao Q, Deng HW (2020) A road map for understanding molecular and genetic determinants of osteoporosis. Nat Rev Endocrinol 16(2):91–103. https://doi.org/10.1038/s41574-019-0282-7

51. Karthik V, Guntur AR (2021) Energy metabolism of osteocytes. Curr Osteoporos Rep 19(4):444–451. https://doi.org/10.1007/s11914-021-00688-6

52. Wei W, Liu X, Chen J, Gao S, Lu L, Zhang H, Ding G, Wang Z, Chen Z, Shi T et al (2017) Class I histone deacetylases are major histone decrotonylases: evidence for critical and broad function of histone crotonylation in transcription. Cell Res 27(7):898–915. https://doi.org/10.1038/cr.2017.68

53. Yu Y, Newman H, Shen L, Sharma D, Hu G, Mirando AJ, Zhang H, Knudsen E, Zhang GF, Hilton MJ et al (2019) Glutamine metabolism regulates proliferation and lineage allocation in skeletal stem cells. Cell Metab 29(4):966–978. https://doi.org/10.1016/j.cmet.2019.01.016

54. Hu T, Shukla SK, Vernucci E, He C, Wang D, King RJ, Jha K, Siddhanta K, Mullen NJ, Attri KS et al (2021) Metabolic rewiring by loss of Sirt5 promotes Kras-induced pancreatic cancer progression. Gastroenterology 161(5):1584–1600. https://doi.org/10.1053/j.gastro.2021.06.045

55. He YJ, Deng F, Zhao SJ, Zhong SL, Zhao JH, Wang DD, Chen X, Zhang T, Hou JC, Zhang W et al (2019) Analysis of miRNA-mRNA network reveals miR-140–5p as a suppressor of breast cancer glycolysis via targeting GLUT1. Epigenomics 11(9):1021–1036. https://doi.org/10.2217/epi-2019-0072

56. Guo Y, Chen T, Liang X, Gou S, Xiong J, Cui J, Peng T (2022) Tumor cell derived exosomal GOT1 suppresses tumor cell ferroptosis to accelerate pancreatic cancer progression by activating Nrf2/HO-1 axis via upregulating CCR2 expression. Cells 11(23):3893. https://doi.org/10.3390/cells11233893

57. Somemura S, Kumai T, Yatabe K, Sasaki C, Fujiya H, Niki H, Yudoh K (2021) Physiologic mechanical stress directly induces bone formation by activating glucose transporter 1 (Glut 1) in osteoblasts, inducing signaling via NAD+-dependent deacetylase (Sirtuin 1) and runt-related transcription factor 2 (Runx2). Int J Mol Sci 22(16):9070. https://doi.org/10.3390/ijms22169070